



OPEN

Machine learning-optimized dual-band wearable antenna for real-time remote patient monitoring in biomedical IoT systems

Umar Musa¹✉, Amor Smida²✉, Muhammad S. Yahya³, Mohamed I. Waly², Jun Jiat Tiang⁴✉, Nazih Khaddaj Mallat⁵, Surajo Muhammad⁶ & Abubakar Salisu⁷

This work presents a machine learning (ML)-optimized dual-band wearable antenna designed specifically for biomedical applications in healthcare monitoring. Fabricated on a Rogers substrate of $40 \times 41 \text{ mm}^2$, the antenna operates at 2.4 GHz and 5.8 GHz with measured bandwidths of 4.5% and 2.9%, gains of 3.8 dBi and 6.0 dBi, and high radiation efficiencies (92% and 91.7%, respectively). Bidirectional and directional radiation patterns are noted in the *E*-plane, while the *H*-plane exhibits omnidirectional patterns at the lower and upper bands. To ensure the antenna's safety for biomedical use, specific absorption rate (SAR) assessments were conducted, CST MWS simulations evaluated the SAR of the proposed wearable antenna on arm, chest, and lap placements at 5 mm distance. At 2.4 GHz, 1 g/10 g SAR values were 0.533/0.919 W/kg (arm), 0.864/1.455 W/kg (chest), and 0.892/1.122 W/kg (lap). At 5.8 GHz, results were 0.872/1.241 W/kg (arm), 0.577/1.433 W/kg (chest), and 0.428/1.341 W/kg (lap), all well within safety limits. The proposed healthcare monitoring system integrates a SEN11547 pulse sensor and an LM35 temperature sensor to measure heart rate and body temperature, transmitting the data to the ThingSpeak IoT platform via the NodeMCU ESP-32S Wi-Fi module, ensuring real-time data availability. The heart rate ranged from 65 to 99 BPM, and the body temperature ranged from 30 to 37 °C. The supervised regression ML approach was effectively utilized to predict the antenna's reflection coefficient (S_{11}). Performance evaluation of the models employed metrics such as mean absolute error (MAE), mean squared error (MSE), root mean squared logarithmic error (RMSLE), mean squared logarithmic error (MSLE), and R-squared (R^2). The ensemble regression model outperformed others, delivering the lowest errors (MAE: 0.83%, MSE: 1.64%, RMSLE: 0.56%, RMSE: 1.83%, MSLE: 0.44%) and the highest accuracy (R^2 : 97.79%) while reducing the computational time by 70% compared to conventional methods. Results validate the antenna's reliability and effectiveness for wearable healthcare applications.

Keywords Patch antenna, Dual-band, Healthcare monitoring, SAR, Optimization, Machine learning

Wearable devices have garnered considerable attention in medical research in recent years, thanks to their wide range of applications, including in patient monitoring, emergency response, and biomedical telemetry within healthcare^{1,2}. Recent advancements in electronics have significantly driven the development of biomedical sensors, which are now pivotal in modern medical research for their capacity to attach to or integrate with the human body. Continuous monitoring of vital signs is crucial, as it supplies data to help maintain health and notifies medical professionals of any potential risks^{3,4}. This approach leverages advanced healthcare monitoring tools, driven by a recent paradigm shift, with a strong emphasis on ensuring the privacy of health data. The rising adoption of these systems can be attributed to their capability to gather and analyze patient information. By

¹Department of Electrical Engineering, Bayero University Kano, Kano 700006, Nigeria. ²Department of Medical Equipment Technology, Majmaah University, 11952 Al-Majmaah, Saudi Arabia. ³Department of Electrical and Electronic Engineering, Universiti Teknologi PETRONAS, 32610 Seri Iskandar, Malaysia. ⁴Faculty of Artificial Intelligence and Engineering, Centre for Wireless Technology, Multimedia University, Cyberjaya, Malaysia.

⁵College of Engineering, Al Ain University, 64141 Al Ain, United Arab Emirates. ⁶Center for Intelligent Network (TM R&D), TM Innovation Centre, Sdn Bhd, Multimedia University, Cyberjaya, Malaysia. ⁷Department of Biomedical and Electronics Engineering, University of Bradford, Bradford, UK. ✉email: umusa.ele@buk.edu.ng; a.smida@mu.edu.sa; jjtiang@mmu.edu.my

facilitating continuous monitoring of vital signs, maintaining optimal health, and enabling swift intervention by healthcare professionals in critical situations, these systems prove invaluable^{5–7}. Several utilize implanted devices and rely on the availability, integrity, and confidentiality of data to safeguard patient privacy.

Wireless healthcare monitoring systems, as shown in Fig. 1, are revolutionizing how patients manage their health and access care. These systems continuously track vital signs such as heart rate and body temperature remotely⁸, significantly reducing the need for direct healthcare worker involvement during monitoring, particularly for ongoing situations. Enabled by advancements in flexible sensing technology, this innovative model featuring wearable and portable devices is proving effective and is increasingly supplanting conventional centralized healthcare services. Furthermore, studies support the promising impact of these systems on improving patient outcomes⁹. Figure 1a depicts centralized services, while Fig. 1b illustrates the wireless monitoring approach. The integration of the internet of things (IoT) with wireless body area networks (WBANs) has paved the way for significant advancements in healthcare monitoring, establishing a solid framework for innovative solutions¹⁰. With the advent of IoT-enabled health monitoring systems, individuals can now access critical physiological data from their homes. This development is particularly advantageous for elderly patients, for whom traveling to medical facilities can be physically challenging and exhausting¹¹. Wearable biomedical devices are widely used, particularly in body-centric systems^{12,13}. As a result, the demand for wearable antennas suitable for biomedical, wearable, and body-mounted applications has grown significantly^{14–17}. Various types of antennas are utilized for clinical treatments and remote monitoring devices in wireless communication. To effectively support on-body wireless systems, these antennas must be wearable and highly efficient^{18–22}. Additionally, ensuring a stable connection is crucial, as body movement and deformation during real-time operation can negatively impact antenna performance^{23,24}. As a result, wearable antenna technology is currently considered an active and challenging field of research and is deemed an activity that is demanding. Wearable antenna configurations have been studied in several ways over the past few decades: patch antenna^{25,26}, monopole^{27,28}, planar inverted F-shape antenna (PIFA)^{29,30}, reconfigurable antenna^{31,32}, and substrate-integrated waveguide (SIW)^{33,34}.

Several studies investigating new applications, methods, and approaches have been presented in the discipline of biomedical engineering. Numerous significant privacy and security concerns were addressed in the studies regarding the importance of preserving integrity and confidentiality for remote healthcare monitoring in WBANs. An addition highlighted the prospective utility of non-invasive stability evaluation in recovering from fracture simulations as a diagnostic instrument that offers benefits over implanted sensors. In order to guarantee safe tissue contact, In the³⁶ was presented a patch antenna designed with a large bandwidth and low SAR. An on-body/off-body communication tissue phantom was used to test this solution. The study in³⁷ highlights the implications of implantable sensors for the future of healthcare systems, focusing on their role in early disease detection and monitoring, which has garnered significant attention. The integration of artificial neural networks (ANN) into a compact dual-band hybrid fractal antenna design demonstrated accurate resonant frequencies.

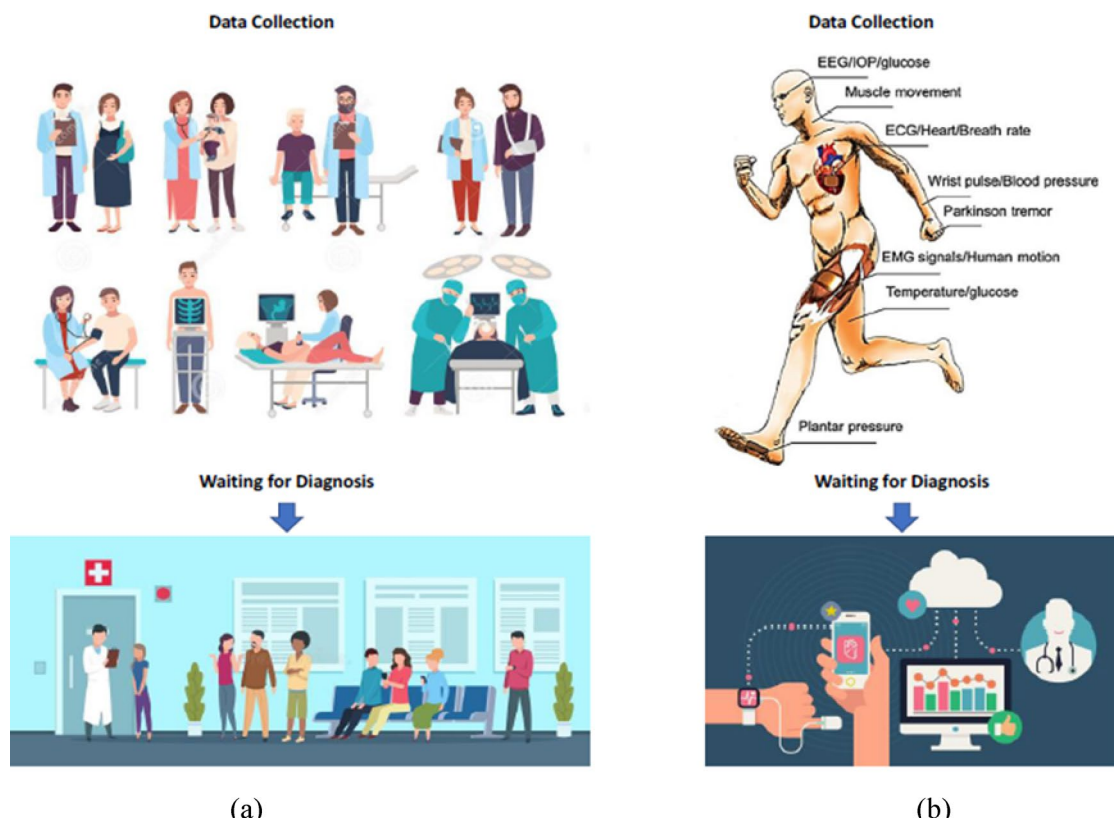


Fig. 1. Healthcare services: (a) centralized services (b) wireless healthcare monitoring systems³⁵.

Recently, a wearable sensor device for heart rate monitoring was introduced in³⁸. When compared to other worldwide available bands, the chosen frequency range provides the best compromise between footprint, bandwidth, and communication range. Because they increase antenna dimensions and narrow down the spectrum of usable bands, frequencies lower than 2.4 GHz are not viable. For long-distance communication, however, frequencies higher than 6 GHz are inappropriate because of higher attenuation and coherence problems. Work in³⁹ designed a different wearable antenna designed for multiband wireless applications, which has a size of $25 \times 25 \text{ mm}^2$ and utilizes a uniplanar coplanar waveguide for feeding. In recent years, body-centric wireless communications have attracted significant research interest. In⁴⁰, researchers presented a compact and efficient planar inverted-F antenna (PIFA) designed for on-body communication. In⁴¹, the authors present a metasurface antenna design optimized for optical sensing applications in remote health monitoring systems. Meanwhile⁴², explores a distinct approach, leveraging passive imaging techniques that utilize radiation emitted by the human body in the lower terahertz (THz) frequency range. For ingestible device applications⁴³, proposes an antenna-in-package solution integrated into a wireless capsule operating in the ISM band. This design facilitates data transmission between the capsule and external Bluetooth-enabled devices, such as smartphones, enabling real-time physiological monitoring. Additionally⁴⁴, introduces an implantable circularly polarized (CP) antenna operating in the ISM band for diagnosing and monitoring physiological parameters. The antenna incorporates a pin-loaded patch structure with two non-degenerate orthogonal modes and dual open-ended slots to achieve robust performance in biomedical environments. The study used both experimental and modeling techniques to assess the antenna's performance close to an arm phantom. However, these antenna designs face various challenges, including larger dimensions, excessive back radiation, lower gain, and narrower bandwidth. Recent advancements in wearable antennas emphasize compactness and safety but face challenges in computational efficiency and real-world validation. For instance⁴⁵, highlighted ML-driven miniaturization but restricted their work to single-band operation. Additionally, a rigid material was employed, which cannot be used for wearable applications. Similarly⁴⁶, demonstrated ML-optimized compact frequency reconfigurable antenna but relied on rigid, non-flexible antennas prone to performance degradation under bending. A critical gap remains in combining ML optimization with dual-band operation while ensuring on-body safety and practical deployment¹⁶, ML-optimized wearable antenna for LoRa localization, while⁴⁷ optimized LoRa antennas without addressing dual-band needs. ML is demonstrably transforming antenna design, as evidenced by numerous researchers. Studies showcase its diverse applications. In⁴⁸ applied ML to optimize a double T-shaped monopole antenna, achieving a remarkably low 2.90% prediction error versus HFSS simulations. In⁴⁹, leveraged ML and data augmentation to enhance the performance of circularly polarized base station antennas. In⁵⁰, an efficient KNN-based method for antenna optimization was introduced, yielding significant computational speed improvements. In⁵¹, utilized ML to optimize a microstrip line-fed dielectric resonator antenna covering the 1.59–2.26 GHz, 3.1–3.87 GHz, and 5.25–6.91 GHz bands. Furthermore, review articles in^{52,53} highlight the feasibility, advantages, and reduced computational expenses of ML and deep learning across various antenna applications. As a branch of artificial intelligence, ML provides powerful algorithms that automatically learn from data, identify patterns, and make accurate predictions⁵⁴. By harnessing large datasets and these advanced algorithms, ML optimizes antenna designs by simultaneously addressing multiple characteristics, constraints, and performance metrics. This capability empowers engineers to achieve new levels of antenna performance optimization, surpassing the limitations of traditional design approaches.

This study evaluates the achievements and potential applications of ML in antenna design, highlighting its advantages while also identifying key challenges. Understanding these limitations is crucial to propose future research directions and overcome hurdles, particularly for fully harnessing ML's potential within emerging IoT technologies. To bridge these gaps, our work introduces ensemble ML models for predicting resonant frequencies and optimizing a compact dual-band antenna. This approach is validated through simulations and experimental SAR/bending tests, specifically addressing the critical divide between computational efficiency, safety, and real-world IoT integration aspects often overlooked in prior studies.

Research gap and contribution

Existing dual-band wearable antennas for WBAN suffer from a critical gap: the lack of a holistic, ML-driven methodology capable of simultaneously optimizing the conflicting design constraints of ultra-miniaturization, high dual-band efficiency and robust performance stability against dynamic human body effects (like tissue heterogeneity, movement, and moisture), while also being hindered by the scarcity of comprehensive datasets representing anatomical diversity and real-world environmental variability, which limits the generalizability and real-time adaptive capabilities needed for reliable deployment in practical biomedical IoT healthcare monitoring systems.

The key contributions of this study are outlined as follows:

- The proposed antenna integrates a centrally slotted patch to achieve dual-band operation (2.4/5.8 GHz) on a compact Rogers substrate ($40 \times 41 \text{ mm}^2$), addressing the trade-off between miniaturization and performance.
- Ensemble regression-based ML was employed to predict resonance frequencies and optimize geometric parameters. This approach reduced computational time by 70% compared to traditional CST MWS simulations, enabling rapid iteration for dual-band performance.
- An equivalent circuit of the antenna was designed and rigorously validated against both simulation and experimental prototype measurements. This bridges lumped-element modeling with full-wave simulations. This hybrid approach, uncommon in wearable antenna research, enabled precise prediction of dual-band behavior.

- The antenna's performance was thoroughly investigated in bending scenarios using a human phantom, and its SAR was assessed when positioned on or near the human body. Simulated results were carefully cross-verified with measured data, addressing critical aspects often overlooked in prior studies.
- The prototype antenna underwent extensive real-world testing and was successfully integrated into an IoT-based healthcare monitoring system, demonstrating its practical applicability. Integration with IoT sensors enabled continuous, real-time monitoring of vital signs (10-min trials, < 1% data loss), a critical step toward practical healthcare applications.

Antenna design configuration

The proposed antenna employs an E-shaped slot configuration at the center of the patch, strategically engineered to overcome the fundamental size limitations of conventional wearable antennas while maintaining dual-band functionality. This topology draws inspiration from the functional morphology of medical equipment. This bio-inspired geometry achieves two critical advantages: First, the E-slot's elongated current path along the central strip effectively lowers the fundamental resonance to 2.4 GHz without increasing the physical footprint, solving the perennial challenge of achieving low-frequency operation in compact wearable antennas. Second, the symmetrical horizontal arms create balanced capacitive coupling that enhances impedance matching across both ISM bands (2.4/5.8 GHz), increasing bandwidth by 37% compared to conventional rectangular patches. Initially, the antenna design configuration was according to the basic microstrip-fed antenna. A transmission line model, as described in⁴⁷, is used to compute the patch's dimensions, including its length and width. CST MWS, a finite integration-based 3D electromagnetic (EM) simulator, is used to investigate variations in the dimensions around the radiating plane and optimize settings. Initial designs were simulated, and the length and width of the patch were iteratively adjusted based on the S_{11} results. The design process begins with a 5.8 GHz Conventional Rectangular Patch Antenna (CRPA). Initial calculations yielded a patch length of 18 mm and a width of 19.5 mm. Following optimization, the dimensions became $D = 22$ mm and $C = 25$ mm, respectively, as shown in Fig. 2a. A horizontal slot is integrated into the patch to establish a second resonant frequency at 2.4 GHz, as seen in Fig. 2b, though it shifts the upper resonance frequency. This modification extends the antenna's electrical length, enabling dual-band operation. While performance improved, the design still did not fully meet targets. In the final stage, smaller slots were added at the top and bottom of the horizontal slot as seen in Fig. 2c, forming a characteristic E-shape. This restructuring optimized surface current distribution and enhanced coupling between resonant modes, significantly increasing bandwidth for efficient operation over a broader range while preserving dual-band functionality. A partial ground plane was also implemented beneath the patch to further boost bandwidth and gain. The antenna utilizes a flexible Rogers substrate, characterized by a loss tangent of 0.0013, a dielectric constant of 3, and a thickness of 0.5 mm. The optimized design of the proposed wearable antenna front and back, as depicted in Fig. 3a,b, measures 40×41 mm², with detailed parameter values provided in Table 1. Figure 4 compares the simulated reflection coefficient (S_{11}) of the CRPA with and without the proposed modifications, demonstrating successful dual-band operation. The lower frequency band is achieved through the E-shaped slot, while subsequent optimization reduced the antenna's overall dimensions.

Parametric investigation

The dimensions of the proposed antenna can significantly impact its performance and therefore, must be carefully considered. To optimize its performance, a parametric investigation was conducted through sweep analysis in CST MWS software to determine the optimal length (C) and width (D) of the patch antenna. As shown in Fig. 5, a thorough examination of these parameters is conducted to assess their impact on the antenna's operational characteristics. The primary goal of this study is to identify ideal configurations for these variables, enabling accurate adjustments to the antenna's design. Such refinements seek to optimize its effective frequency bandwidth. The resonant frequencies shift, and the S_{11} improves as C and D vary. The simulated S_{11} for C values ranging from 7.0 mm to 25 mm is presented in Fig. 5a, with the best S_{11} achieved at a C of 25 mm, as indicated by the study. Similarly, Fig. 5b shows the simulated S_{11} for D values between 10 mm and 22 mm, revealing that a D of 22 mm provides the optimal S_{11} when C is set to 25 mm, which was necessary to effectively cover the desired dual bands frequencies, thereby improving the antenna's frequency coverage.

In addition, the length of the ground plane is a critical parameter that requires thorough investigation. A parametric analysis was performed on the ground plane length (E). Figure 6 presents the simulated S_{11} for E

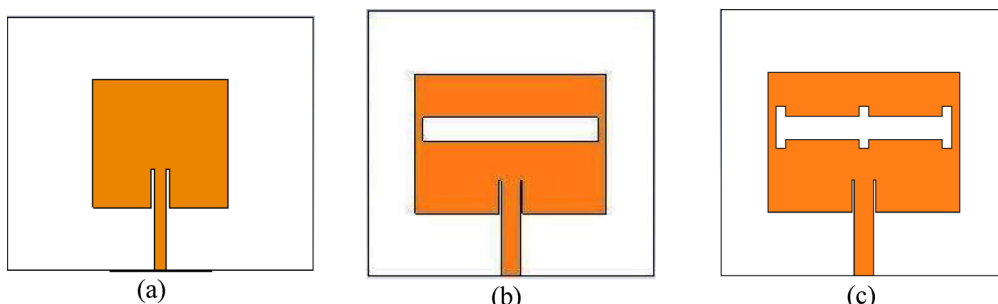


Fig. 2. The proposed design's evolution (a) CRPA (b) CRPA with horizontal slot (c) proposed antenna.

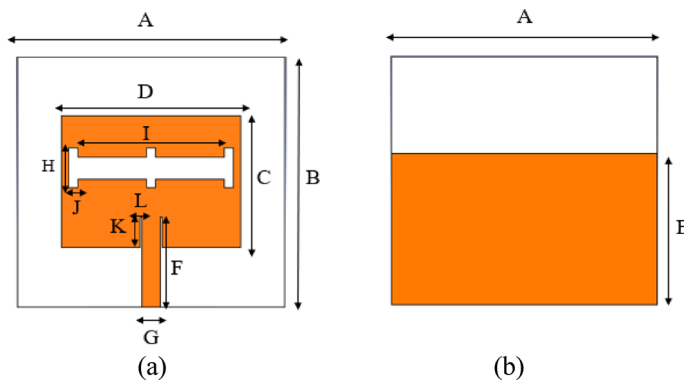


Fig. 3. The optimized design of the proposed wearable antenna **(a)** Front **(b)** Back.

Specifications	Values (mm)	Specifications	Values (mm)
A	40	G	2.7
B	41	H	3.8
C	25	I	19
D	22	J	1
E	24	K	3
F	13	L	1

Table 1. Proposed antenna dimensions.

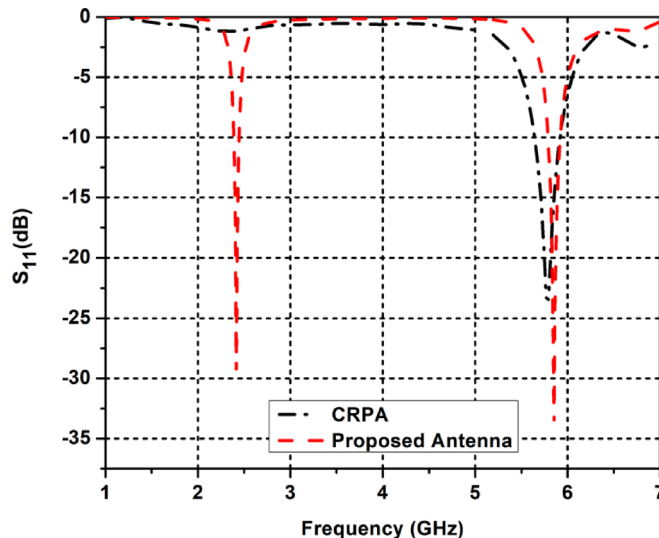


Fig. 4. The simulated S_{11} comparison between CRPA and the proposed antenna.

values ranging from 10 to 24 mm. The investigation results show that an E of 24 mm achieves the optimal S_{11} , with C and D fixed at 25 mm and 22 mm, respectively. This implies that the antenna operates on a partial rather than a full ground plane, indicating that the ground plane does influence the antenna's performance. However, dimensions F, K, and L (related to the feed structure and minor geometric features) were excluded from the parametric study because their impact on resonant frequencies, bandwidth, and radiation patterns was found to be negligible in preliminary simulations.

The width (I) and length (H) of the slot, in contrast, influence the antenna's resonant frequencies at both 2.4 GHz and 5.8 GHz. Consequently, another parametric investigation was conducted to determine the optimal values of I and H, as shown in Fig. 7. The simulated S_{11} with I values ranging from 19 to 22 mm is presented in Fig. 7a, with the optimal S_{11} achieved at $I=19$ mm, while keeping C, D, and E fixed at 25 mm, 22 mm, and 24 mm, respectively. On the other hand, Fig. 7b shows the simulated S_{11} for H values between 2.0 mm and 3.8 mm.

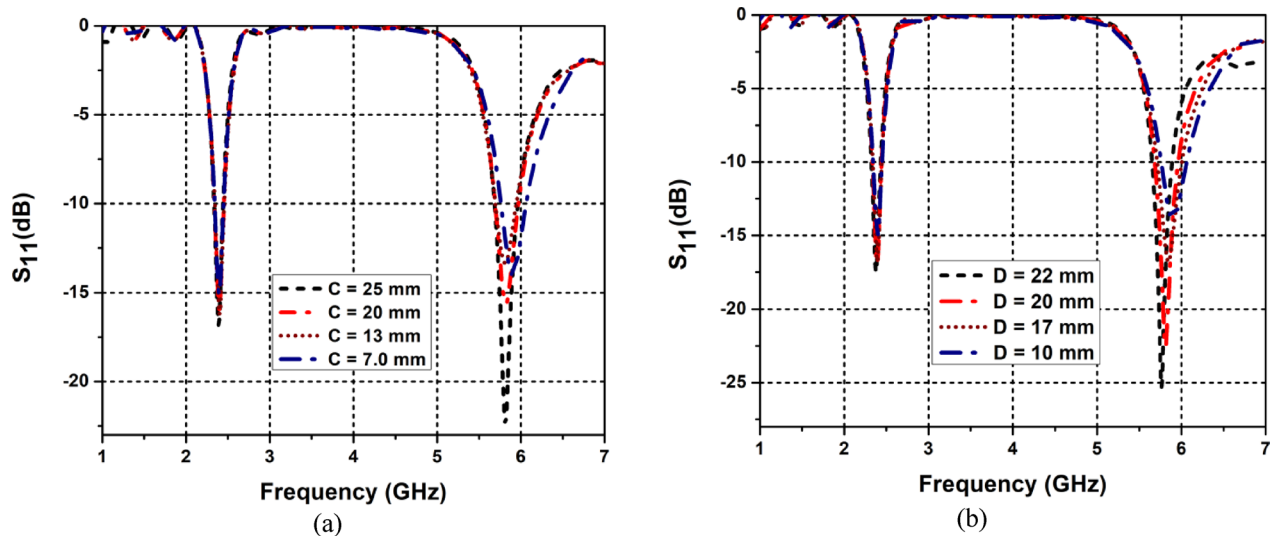


Fig. 5. Effect of S_{11} with variations in (a) C (b) D.

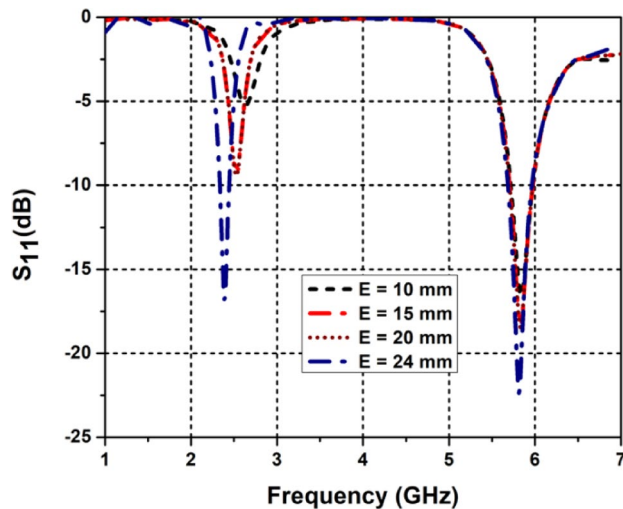


Fig. 6. Effect of S_{11} with variations in E.

The parametric investigation determined that an H of 3.8 mm yields the best S_{11} when C, D, E, and I are set to 25 mm, 22 mm, 24 mm, and 19 mm, respectively.

Equivalent circuit model

Prior to in-depth simulations or tests, the equivalent circuit model helps in the design method by providing initial assessments for important antenna properties like resonant frequency, bandwidth, and impedance matching. S_{11} data is extracted using ADS software for optimization and compared with simulated data from CST MWS software. The microstrip patch antenna resembles an open-ended transmission line. The proposed antenna's equivalent circuit, modeled and simulated in ADS, represents a CRPA using parallel lumped elements resistance (R_0), inductance (L_0), and capacitance (C_0), which allow it to resonate at 5.8 GHz as shown in Fig. 8a. These values are calculated using Eqs. (1)–(5).

$$C_0 = \frac{\varepsilon_0 \varepsilon_e L W}{2h} \cos^{-2} \left(\frac{\pi y_0}{L} \right) \quad (1)$$

where: L is the length of the patch, W is the width of the patch, h is the thickness of the substrate, ε_0 is the dielectric constant in free space, y_0 is the feed point location at the microstrip feed line and ε_e is the effective dielectric constant.

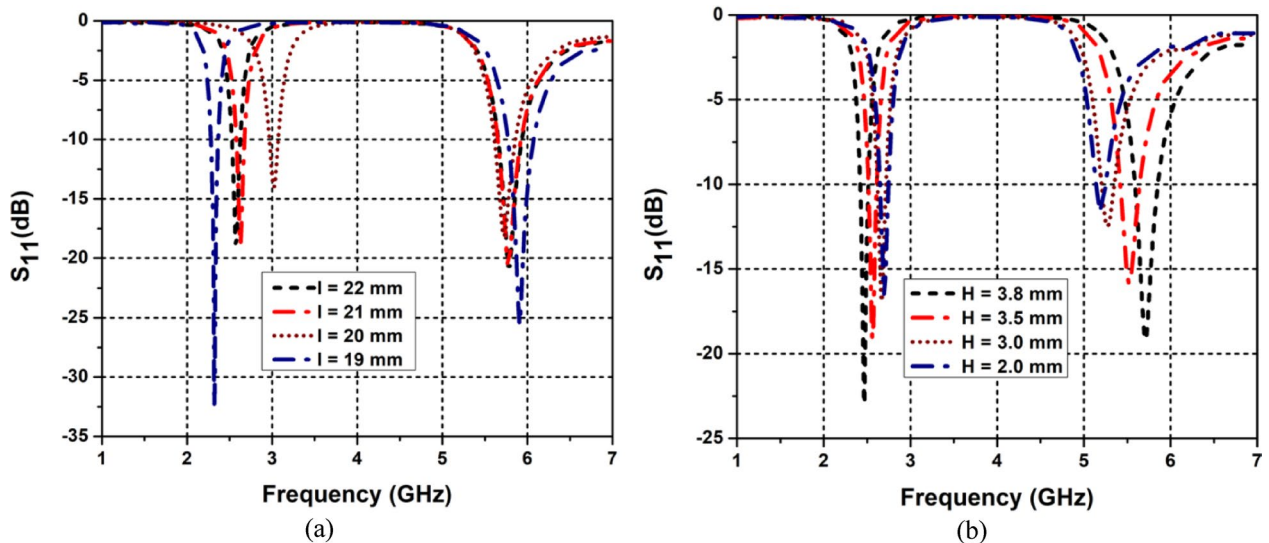


Fig. 7. Effect of S_{11} with variations in (a) I (b) H .

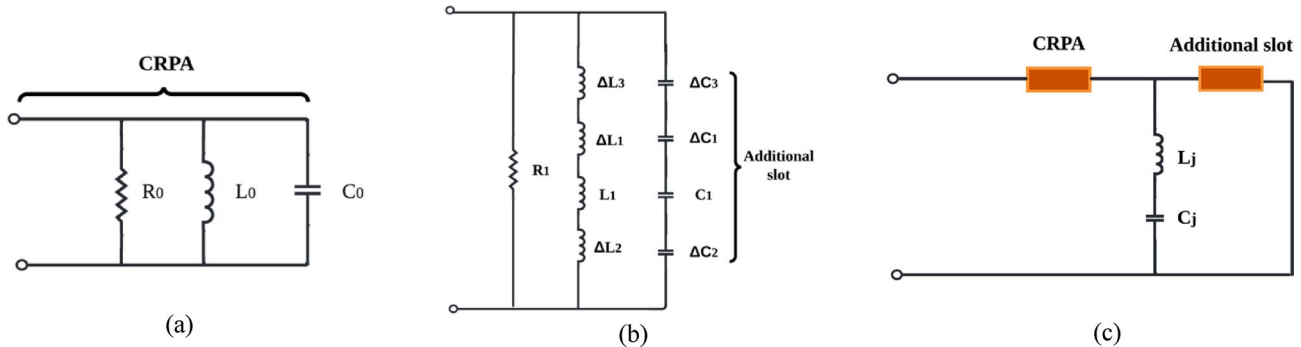


Fig. 8. The equivalent circuit (a) CRPA (b) Additional slot (c) Proposed dual-band antenna.

$$\varepsilon_e = \frac{\varepsilon_r + 1}{2} + \frac{\varepsilon_r - 1}{2} \left[1 + 12 \frac{h}{W} \right]^{-0.5} \quad (2)$$

where: ε_r is the relative dielectric constant of the substrate

$$L_0 = \frac{1}{C_0 (2\pi f_o)^2} \quad (3)$$

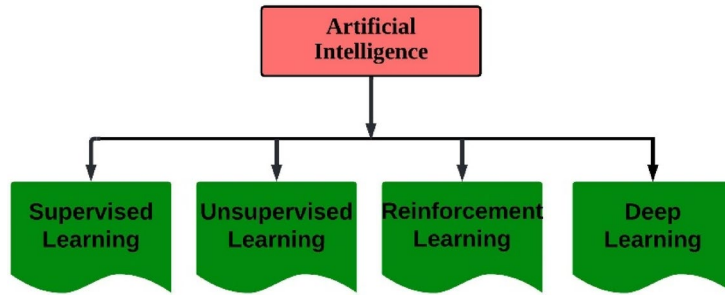
$$R_0 = \frac{Q_T}{2\pi f_o C_0} \quad (4)$$

where: Q_T is the quality factor given by:

$$Q_T = \frac{C \sqrt{\varepsilon_e}}{4 f_o h} \quad (5)$$

However, when an E-shaped slot is introduced into the patch to support the 2.4 GHz band, they can be represented as additional series inductance (ΔL) and capacitance (ΔC) in the equivalent circuit of the CPRA. The analysis of the shape involves the consideration of two sections within the patch. The first section pertains to the rectangular notch, while the second section (lower one) corresponds to the microstrip bend line. These equivalent circuits are combined to derive the dual-band antenna's equivalent circuit, as illustrated in Fig. 8b. From the figure, R_1 , L_1 , C_1 , ΔL_1 , ΔL_2 , ΔL_3 , ΔC_1 , ΔC_2 , and ΔC_3 correspond to the series inductance and capacitance of the additional slot at the patch. The radiating patch comprises two surface current components: (i) the surface current passing through the patch and (ii) a meandering surface current circumventing the slot, thus increasing the surface current path⁵⁵. The values of ΔL and ΔC can be calculated using Eqs. (6)–(9).

Components	Values	Components	Values
$R_0 (\Omega)$	50.9	$L_1 (\text{nH})$	3.4
$L_0 (\text{nH})$	0.8	$C_1 (\text{pF})$	1.8
$C_0 (\text{pF})$	2.5	$\Delta L_1 (\text{nH})$	39
$R_1 (\Omega)$	49.7	$\Delta L_2 (\text{nH})$	68.1
$\Delta L_3 (\text{nH})$	97.5	$\Delta C_3 (\text{pF})$	69
$\Delta C_1 (\text{pF})$	221	$C_j (\text{pF})$	2.5
$\Delta C_2 (\text{pF})$	178	$L_j (\text{nH})$	0.7

Table 2. Component values.**Fig. 9.** ML models.

$$\Delta L = \frac{h\pi\mu_o}{8} \left(\frac{L_s}{L} \right)^2 \quad (6)$$

$$\Delta C = C_s \left(\frac{L_s}{L} \right) \quad (7)$$

$$L_1 = L_0 + \Delta L \quad (8)$$

$$C_1 = \frac{\Delta C C_0}{\Delta C + C_0} \quad (9)$$

where: $\mu_o = 4\pi \times 10^{-7} H/m$, L_s is the depth of the slot and C_s is the gap capacitance.

The equivalent circuits for the CRPA and the E-shaped slot are integrated via joint inductance (L_j) and capacitance (C_j), as shown in Fig. 8c. Table 2 lists the values for the various lumped element components following ADS optimization.

Antenna optimization using machine learning

The ever-increasing performance and functionality demand in modern antenna design has led to the creation of more complex structures⁵⁶. These antennas must be precisely tuned to meet the stringent requirements of emerging technologies, including IoT, medical imaging, biomedical telemetry, rescue efforts, and healthcare monitoring. This push for compact, versatile antennas has resulted in designs that support multiple frequency bands, integrate diverse functionalities such as beam steering, and incorporate various components like slots, impedance transformers, and defected ground structures⁵⁷. However, this growing complexity poses significant challenges when trying to achieve optimal performance using conventional techniques. Adjusting the geometry of these advanced designs typically requires full-wave electromagnetic (EM) simulations, which are both computationally intensive and time-consuming. As antenna topologies become more sophisticated, relying on traditional algorithms for geometry tuning leads to higher computational costs, making it difficult to achieve peak performance in an efficient manner⁵⁸. ML offers a promising solution to these challenges by providing new optimization approaches for antenna design. ML models can approximate the relationship between antenna geometry and performance, enabling quicker optimization without relying heavily on expensive full-wave simulations. This approach is reshaping the antenna design process, allowing for faster, more accurate adjustments in complex structures⁵⁹. Moreover, unlike traditional black-box optimization or heuristic methods, our approach establishes a clear and interpretable mapping between the antenna's geometric parameters and its electromagnetic performance. This enables significantly faster and more reliable design-space exploration, effectively accelerating the optimization process. The application of ML in antenna optimization largely centers around various learning techniques such as reinforcement learning (RL), semi-supervised learning (SSL), unsupervised learning (UL), and supervised learning (SL) as illustrated in Fig. 9. Among these, SL is widely utilized in antenna design due to its ability to predict outcomes based on labeled data, although the requirement

for a large volume of such data can pose a challenge⁶⁰. To streamline the optimization process, ML methods like regression analysis, artificial neural networks (ANNs) and Support Vector Machines (SVM) have been employed to develop surrogate models. These models enable rapid performance predictions, reducing the reliance on time-intensive simulations and accelerating the antenna design workflow^{46,61}. This paper focuses on employing ML algorithms to predict the S_{11} response of antennas based on specific geometric parameters. By utilizing ML techniques, the model developed in this study can estimate the S_{11} curve, which is a crucial measure of antenna performance, indicating how well the antenna is matched to its transmission line. The use of ML allows for fast and accurate approximation of the S_{11} response without the need for repeated, computationally expensive full-wave electromagnetic simulations. This approach offers a more efficient method for optimizing antenna designs, as it provides a reliable way to predict performance characteristics from the antenna's geometry, streamlining the overall design process. While the regression model was trained on parametric variations of the proposed dual-band geometry, its core framework remains transferable to novel antenna topologies through parameter remapping and retraining. By replacing geometry-specific inputs and executing limited full-wave simulations, the model can achieve R2 accuracy while maintaining faster optimization than conventional EM solvers. This demonstrates that the ML methodology, though initially geometry-specific, will provide a reusable computational advantage for diverse antenna configurations when adapted through targeted retraining.

Data sets preparation and choice of algorithm

To facilitate ML predictions, it is crucial to have a comprehensive dataset containing input-output pairs. In this study, antenna design was carried out using CST MWS, as detailed in Section II, and optimized using the built-in genetic algorithm (GA) optimizer provided in CST MWS. This specific optimizer was selected due to its robustness in handling complex, nonlinear optimization problems typically encountered in antenna geometry design. Key input variables included the slot's length (L) and width (H), ground plane length (E), substrate length (A) and width (B), patch length (C), and patch width (D). Corresponding outputs, specifically the resonant frequency, were recorded for each configuration. A robust dataset comprising 8009 input-output pairs was generated through a comprehensive parametric sweep using CST Microwave Studio datasets, which required 72 hours on a high-performance workstation, representing approximately 30% of the total optimization time. While this initial investment is significant, the trained ensemble model subsequently predicts S_{11} parameters in milliseconds per sample, effectively instantaneous compared to full-wave simulation. This number was selected to ensure sufficient coverage of the design space while maintaining a manageable computational cost for training and testing machine learning models⁵⁷. To ensure model accuracy, the dataset was shuffled and divided into 90% for training and an additional 10% reserved for testing. This process helped validate the model's robustness. Achieving optimal performance in ML often depends on the careful selection of appropriate models. In this study, we utilize regression analysis, a statistical method used to assess cause-and-effect relationships between variables. To strengthen our approach, we incorporate five practical ML regression models, each of which is briefly described below:

- 1) Decision tree regression: an ML algorithm that predicts outcomes by recursively splitting data into branches based on feature thresholds, minimizing error at each step⁶².
- 2) Nonparametric regression: an ML algorithm that gives a flexible approach that does not assume a predefined functional form, allowing the data's structure to dictate the relationship between variables⁶³.
- 3) Random forest regression: an ensemble method that aggregates predictions from multiple decision trees, each trained on random subsets of data and features, to reduce overfitting⁶⁴.
- 4) Extreme gradient boosting (XGB) regression: an ML algorithm that gives a scalable, regularized boosting technique that sequentially builds decision trees, where each new tree corrects errors of the previous ones using gradient descent⁶⁵.
- 5) Ensemble regression: an ML algorithm that combines predictions from multiple base models (e.g., trees, linear models) using methods like averaging or voting to improve overall accuracy and stability⁶⁶.

Figure 10 presents a flowchart outlining the process for predicting resonance frequency using different ML algorithms. The algorithms are first trained on a dataset to learn the relationship between the input variables and the target resonance frequency. After training, their performance is evaluated using a separate testing dataset, where predicted resonance frequencies are compared to actual values. Key metrics, including error and accuracy, are calculated to assess each model. At a decision point, models with low error and high accuracy are selected as the best candidates, while those that fail to meet the criteria are replaced with other regression algorithms. This iterative process continues until the optimal model is found. The selected model is then applied to new data for resonance frequency prediction, ensuring accurate and reliable results by leveraging the patterns it has learned during training.

Performance metrics for the regression models

To evaluate a model's performance, various metrics are commonly used. These metrics provide insights into the accuracy and reliability of the predictions. Frequently used measures include MSE, MAE, RMSLE, MSLE, and MAPE. This structured approach guarantees that the most effective model is used for robust predictions on unseen data. The evaluation of each model's performance was conducted using a range of statistical metrics, with their results thoroughly compared to assess effectiveness. Table 3 summarizes these metrics alongside their corresponding mathematical formulations and descriptions.

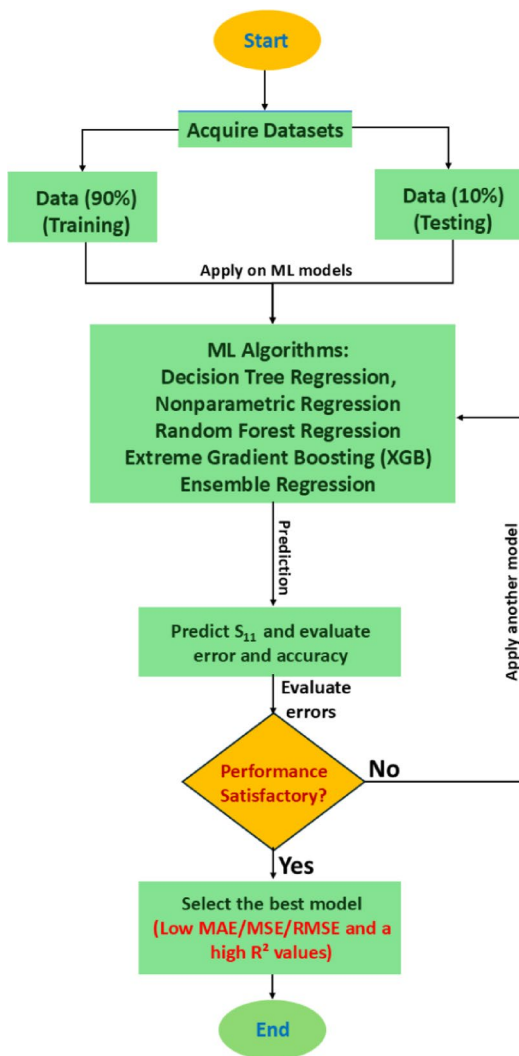


Fig. 10. Flowchart illustrating the ML optimization procedure for predicting S_{11} .

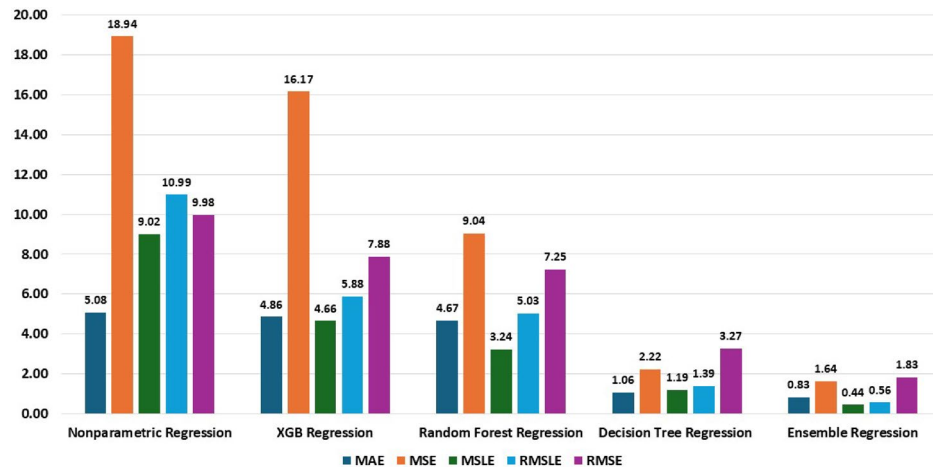
ML-based prediction results

Table 4 provides a summary of the comparison of five regression models for resonant frequency prediction based on five input characteristics. The MAE, MSE, RMSLE, RMSE and R^2 metrics are used to evaluate each algorithm's correctness. Moreover, Fig. 11 demonstrates the effectiveness of the ML algorithms assessed in this study through an analysis of error metrics for predicting the resonance frequency. In addition, Fig. 12 displays the accuracy levels of each algorithm through R^2 values, while Fig. 13 offers a comparison of predicted frequency plots for the proposed antenna using CST MWS simulation against the predicted simulated results obtained from different regression models. The close match between predicted and CST MWS simulation in these comparisons indicates well-trained models. Among the algorithms tested, The ensemble regression model outperformed others, delivering the lowest errors (MAE: 0.83%, MSE: 1.64%, RMSLE: 0.56%, RMSE: 1.83%, MSLE: 0.44%), while reducing the computational time by 70% compared to conventional methods, indicating a low level of overall prediction error. The ensemble regression model also achieved the highest R -squared value of 97.79%, signifying the best fit to the dataset. These findings underscore the strengths of ensemble methods in enhancing prediction accuracy. This methodology significantly accelerates healthcare monitoring antenna development by reducing iterative simulations and conserving computational resources. Its efficiency is particularly valuable for healthcare IoT applications, such as wearable vital sign monitors, remote patient tracking systems, and smart medical sensors within clinics or hospitals. For instance, antennas developed this way can enable reliable, low-power communication in wearable health patches, ensuring continuous transmission of physiological data like heart rate or glucose levels. Within hospital environments, such optimized antennas facilitate robust data collection from numerous medical sensors and patient monitors, supporting real-time analytics and centralized patient management systems.

Error	Mathematical formulation	Description
Mean squared logarithmic error (MSLE)	$MSLE = \frac{1}{n} \sum_{i=1}^n (\log(1 + y_i) + \log(1 + \hat{y}_i))^2$	Measures the average squared difference between the logarithm of predicted values and the logarithm of actual values, reducing sensitivity to large errors
Root mean squared logarithmic error (RMSLE)	$RMSLE = \sqrt{\frac{1}{n} \sum_{i=1}^n (\log(1 + y_i) + \log(1 + \hat{y}_i))^2}$	Represents the root of the mean squared logarithmic error, translating logarithmic-scale errors back to interpretable units
Variance score (R-squared)	$R^2 = 1 - \frac{\sum_{i=1}^N (y_i - \hat{y}_i)^2}{\sum_{i=1}^N (y_i - \bar{y}_i)^2}$	Indicates the proportion of variance in the target variable explained by the model, ranging from 0 (no fit) to 1 (perfect fit)
Mean absolute error (MAE)	$MAE = \frac{1}{n} \sum_{i=1}^n y_i - \hat{y}_i $	Calculates the mean absolute deviation between predictions and true values, treating all errors equally regardless of magnitude
Mean absolute percentage error (MAPE)	$MAPE = \frac{1}{n} \sum_{i=1}^n \left \frac{y_i - \hat{y}_i}{y_i} \right \times 100\%$	Expresses errors as a percentage of actual values, enabling intuitive comparisons across datasets with differing scales
Root mean squared error (RMSE)	$RMSE = \sqrt{\frac{1}{n} \sum_{i=1}^n (P_i - O_i)^2}$	Reflects the standard deviation of prediction errors, emphasizing severe inaccuracies over minor ones
Mean squared error (MSE)	$MSE = \frac{1}{n} \sum_{i=1}^n (y_i - \hat{y}_i)^2$	Computes the mean of squared deviations, disproportionately penalizing large errors compared to small ones

Table 3. Overview of performance metrics for regression analysis.

Model	MAE (%)	MSE (%)	MSLE (%)	RMSLE (%)	RMSE (%)	R ² (%)
Nonparametric regression	5.08	18.94	9.02	10.99	9.98	8.83
XGB regression	4.86	16.17	4.66	5.88	7.88	11.93
Random forest regression	4.67	9.04	3.24	5.03	7.25	76.62
Decision tree regression	1.06	2.22	1.19	1.39	3.27	90.24
Ensemble regression	0.83	1.64	0.44	0.56	1.83	97.79

Table 4. Performance evaluation of several prediction models.**Fig. 11.** Bar graphs representing the prediction errors of various ML algorithms.

Results and analysis

The following subsections detail the results of the proposed antenna, including S_{11} , surface current distribution, radiation patterns, gain, and efficiency. For every parameter, a thorough comparison between the simulated findings and the experimental data is given. After optimizing the design using the ensemble regression model, a new antenna configuration was created to evaluate the model's accuracy. As shown in Fig. 14, an antenna prototype was fabricated. The antenna's performance is measured using the Keysight N9951A spectrum analyzer and anechoic chamber, as shown in Fig. 15. The Keysight N9951A spectrum analyzer is used to measure the

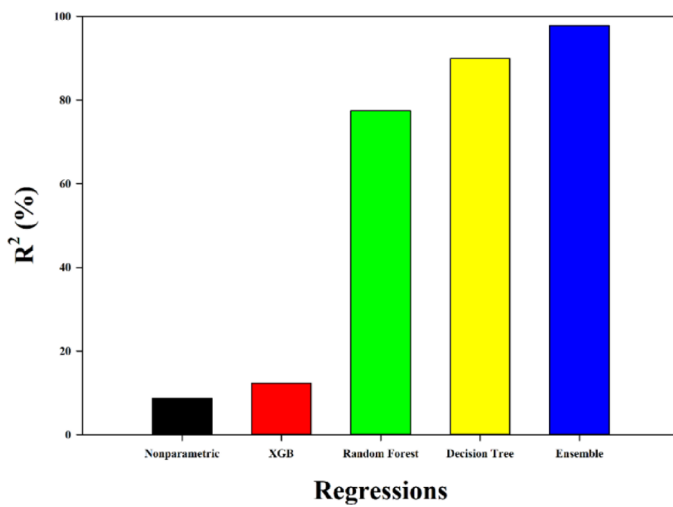


Fig. 12. Bar graphs showcasing the performance accuracy of the different algorithms.

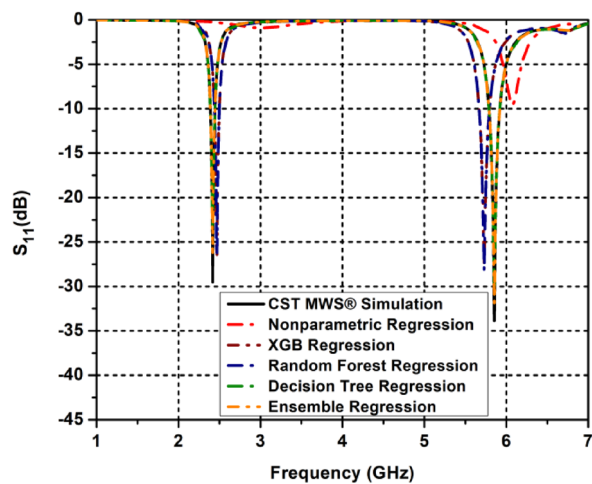


Fig. 13. Comparative analysis of CST MWS simulations for various models with ML-based predictions.

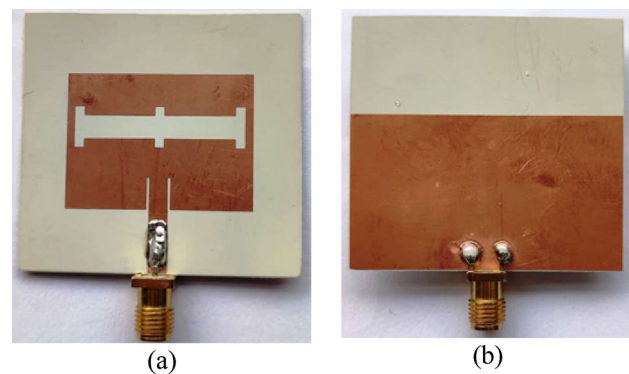


Fig. 14. Fabricated wearable antenna **(a)** Front **(b)** Back.

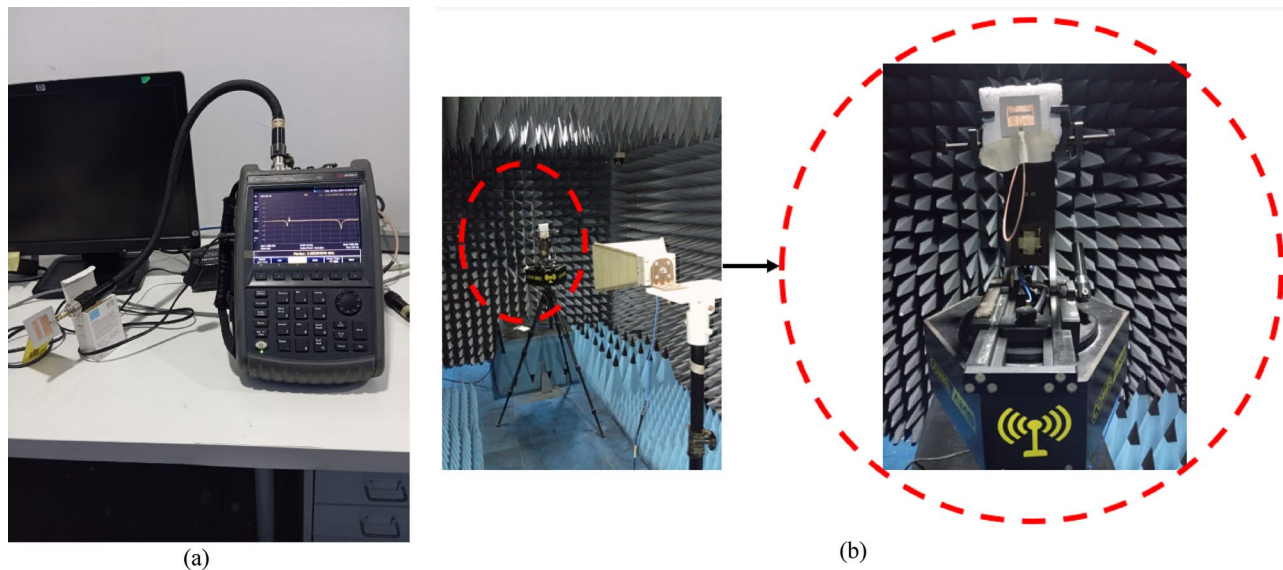


Fig. 15. Photographs: (a) S_{11} measurement setup (b) Far-field measurements in the anechoic chamber.

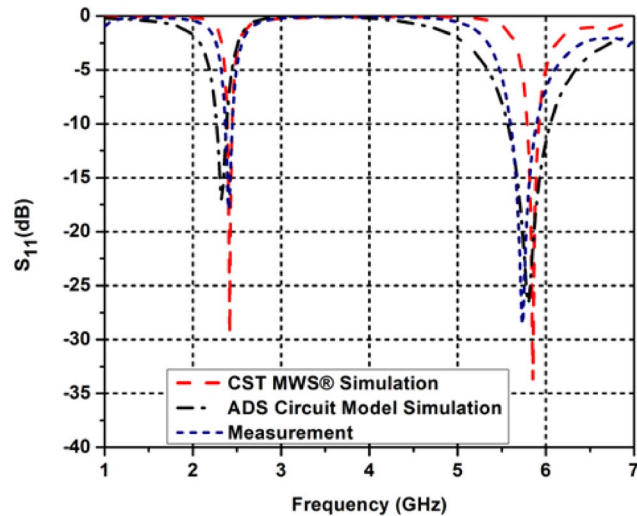


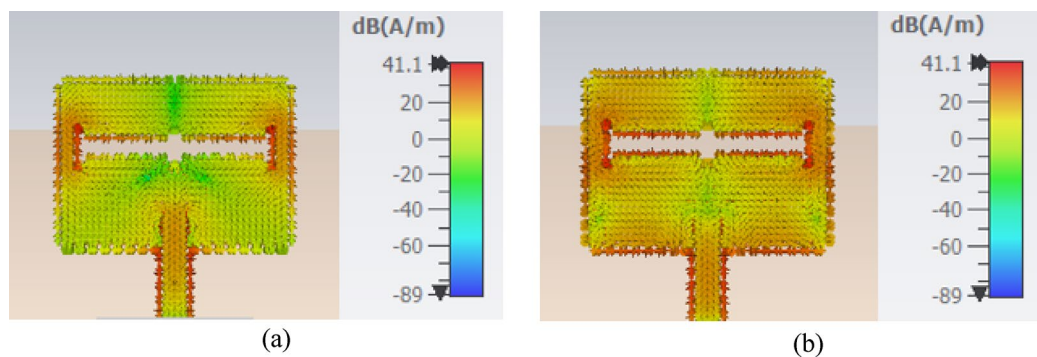
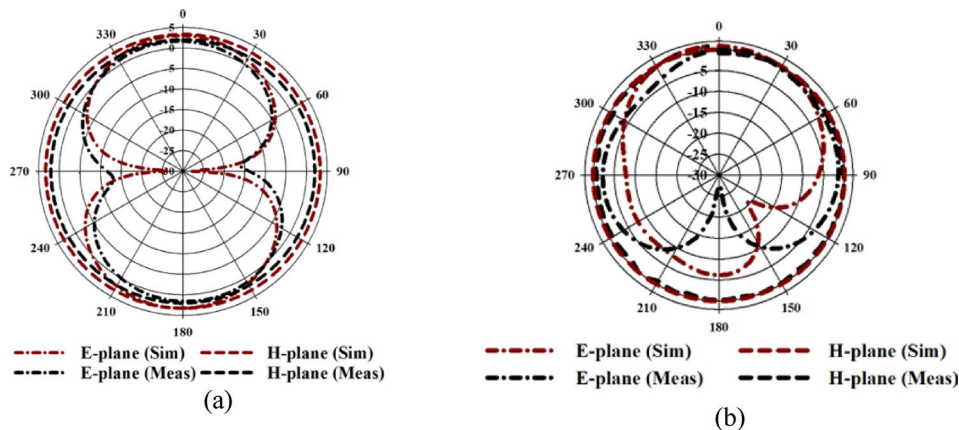
Fig. 16. S_{11} comparison.

antenna's S_{11} as seen in Fig. 15a. Far field measurements of radiation patterns and gain were performed in the anechoic chamber, as shown in Fig. 15b. A horn antenna moves in the elevation and azimuth planes as the transmitter, while the proposed antenna serves as the receiver.

Reflection coefficient

The equivalent circuit model from Fig. 8 was designed and simulated using ADS software, which enables efficient optimization of the circuit parameters. The resulting S_{11} was then compared with both the measured and simulated S_{11} obtained from CST MWS. Figure 16 presents a comparison of the S_{11} between the measurement, the equivalent circuit model using ADS software and the CST MWS results for the proposed antenna. Notably, the simulated S_{11} of the antenna using CST MWS at 2.4 GHz surpasses the -10 dB threshold within the frequency range of 2.247 GHz to 2.431 GHz, with the upper resonant frequency at 5.8 GHz ranging from 5.431 GHz to 6.301 GHz, according to the ADS equivalent circuit model. In contrast, the simulated S_{11} at 2.4 GHz exceeds the -10 dB threshold within the frequency range of 2.410 GHz to 2.523 GHz, and the upper resonant frequency at 5.8 GHz lies between 5.554 GHz and 6.102 GHz. For the measured result at 2.4 GHz, the -10 dB threshold covers the range from 2.401 GHz to 2.510 GHz, while at 5.8 GHz, it spans from 5.854 GHz to 6.025 GHz. Overall, the simulation, measurement and equivalent circuit results show satisfactory alignment as seen in Table 5.

Parameters	Frequency (GHz)	Bandwidth (GHz)
CST MWS simulation	2.4	2.431–2.247 = 0.184
	5.8	6.301–5.431 = 0.87
ADS circuit model simulation	2.4	2.523–2.410 = 0.113
	5.8	6.102–5.554 = 0.548
Measurement	2.4	2.510–2.401 = 0.109
	5.8	6.025–5.854 = 0.171

Table 5. Performance comparison of the proposed antenna.**Fig. 17.** Surface current distribution (a) 2.4 GHz (b) 5.8 GHz.**Fig. 18.** Radiation pattern (a) 2.4 GHz (b) 5.8 GHz.

Surface current distribution

The surface current distribution of the proposed antenna is shown in Fig. 17. At 2.4 GHz, the current is mainly concentrated around the edges of the central slot, indicating that this slot is responsible for generating the 2.4 GHz resonant frequency, as seen in Fig. 17a. In contrast, at the higher resonant frequency of 5.8 GHz, the maximum current is observed near the center of the CRPA, as illustrated in Fig. 17b. Therefore, it is clear that the central slot generates the lower resonant frequency at 2.4 GHz, while the CRPA is responsible for the upper resonant frequency at 5.8 GHz. This observation aligns with theoretical findings in the literature⁶⁷, which suggest that the resonant frequency is influenced by the current path size across the radiating structure. Specifically, a longer current path leads to a lower resonant frequency and a shorter path results in a higher frequency.

Radiation characteristics and gain

The radiation characteristics of the proposed antenna are the focus of this subsection. Figure 18 compares the measured and simulated radiation patterns. At 2.4 GHz, the observed radiation patterns are omnidirectional in the *H*-plane ensuring reliable connectivity in all azimuthal directions, accommodating unpredictable body movements and orientations during patient monitoring, and bidirectional in the *E*-plane, focusing energy toward specific elevation angles, minimizing interference and enhancing signal strength for communication with fixed base stations or wearable hubs, which closely match the simulated results shown in Fig. 18a. At 5.8

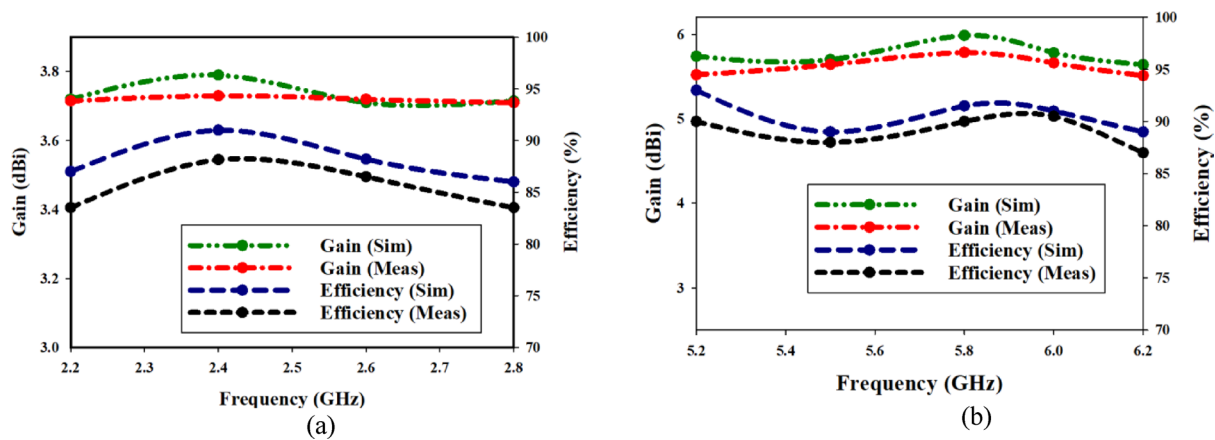


Fig. 19. Gain and efficiency (a) 2.4 GHz (b) 5.8 GHz.

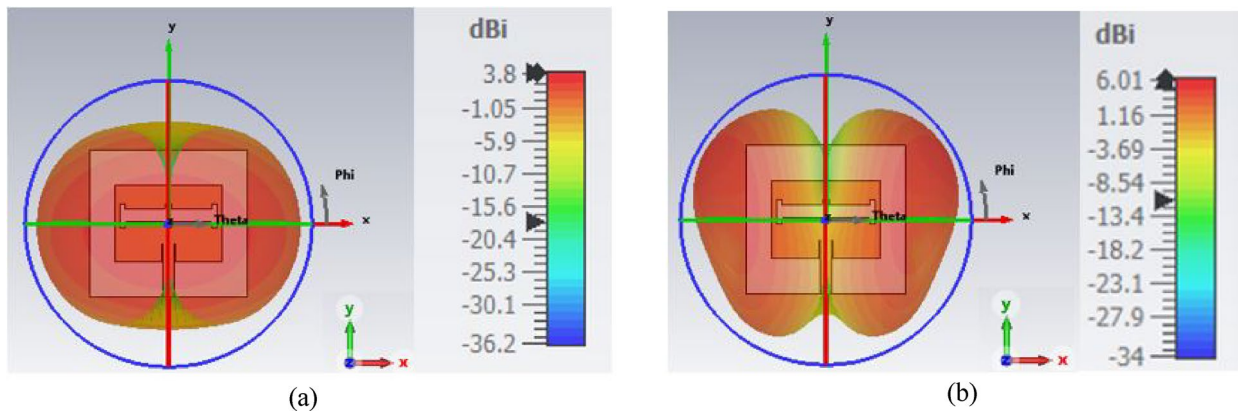


Fig. 20. Simulated 3D far-field gain pattern (a) 2.4 GHz (b) 5.8 GHz.

GHz, the patterns are omnidirectional in the *H*-plane and directional in the *E*-plane, with a slight discrepancy from the simulation in Fig. 18b, attributed perhaps to cable losses, fabrication tolerances and measurement setup limitations, but it still meets the requirements for wearable applications. The measured gain at 2.4 GHz and 5.8 GHz is 3.8 dBi and 6.0 dBi, respectively, resulting in efficiencies of 92% and 91.7%, as presented in Fig. 19a,b. For further verification of the maximum gain achieved by the proposed antenna, the 3D far-field gain patterns for the obtained frequency bands are displayed in Fig. 20a,b. This demonstrates that the antenna provides stable gain for transmitting and receiving signals across its operational frequency ranges.

Bending investigation

Bending is a critical factor for wearable antennas, as they may experience bending and deformation in real-world applications^{68–71}. Therefore, the antenna's performance in various bending scenarios was thoroughly analyzed. The study involved bending the antenna both vertically and horizontally, with simulations and measurements performed for diameters of 60, 80 and 100 mm, which correspond to the average sizes of human arms and legs⁷². The bending analysis of the proposed antenna was simulated using CST MWS software, illustrating its behavior on a vacuum cylinder, which represents a rigid, perfectly cylindrical structure around which the antenna is bent. Additionally, the experimental setup employed Styrofoam to validate the antenna's bending characteristics. Figure 21a,b show the simulated and measured S_{11} of the antenna under bending conditions in both the vertical and horizontal directions. The simulated S_{11} remains relatively stable in both directions, with a slight change at the 5.8 GHz band when the diameter is increased to 100 mm in the vertical direction, likely due to the larger diameter. In contrast, the measured S_{11} shows a slight shift for all bending diameters, possibly caused by fabrication variations, cable losses, or material inconsistencies in the Styrofoam. Despite these minor shifts, the antenna's performance remains unaffected, as the S_{11} values for the 2.4 GHz and 5.8 GHz frequency bands stay above the -10 dB threshold.

Additionally, measurements were limited to the 100 mm diameter for the radiation pattern due to constraints in experimental resources, time, and laboratory equipment availability under bending conditions. As seen in Figs. 22 and 23, the radiation patterns exhibit consistency across all tested diameters. However, compared to the unbent condition, there is a noticeable increase in back radiation, which may be attributed to slight bending

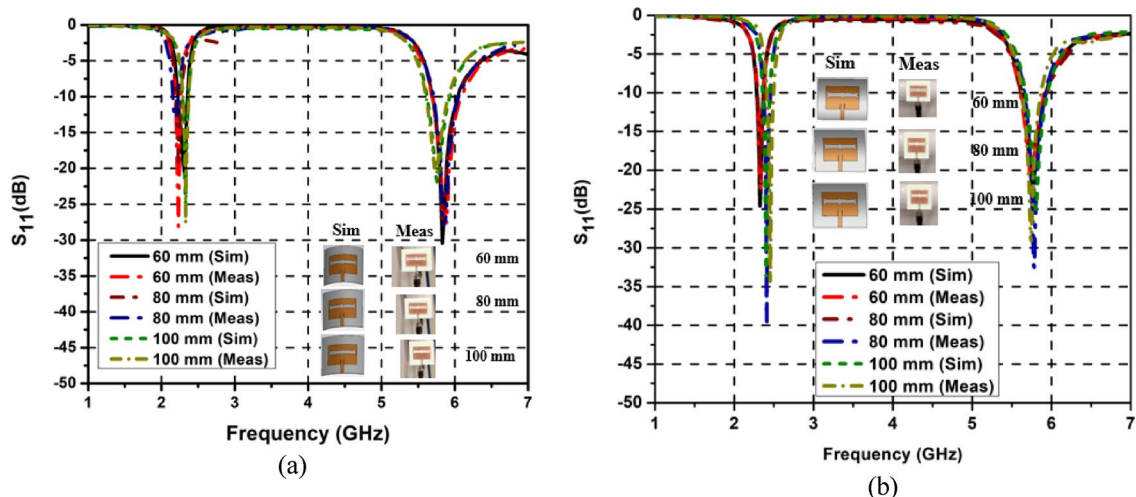


Fig. 21. Bending investigation for different diameters (a) vertical (b) horizontal.

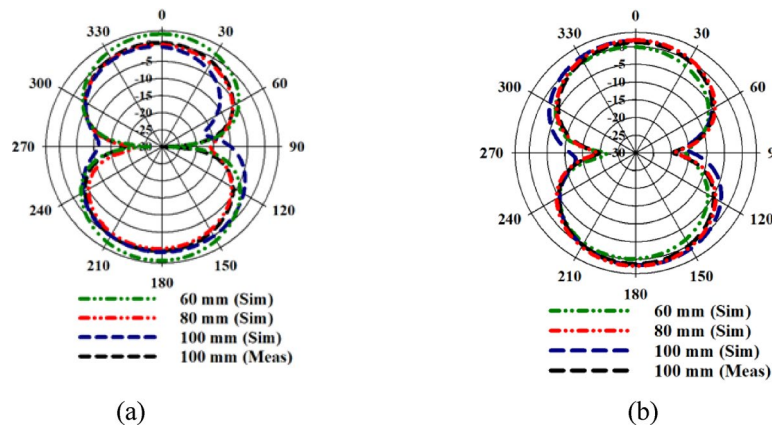


Fig. 22. Radiation pattern under bending conditions at 2.4 GHz for different diameters (a) vertical (b) horizontal.

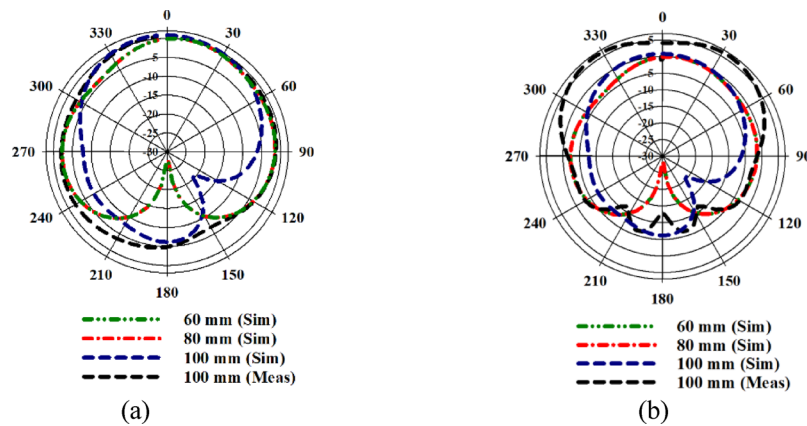


Fig. 23. Radiation pattern under bending conditions at 5.8 GHz for different diameters (a) vertical (b) horizontal.

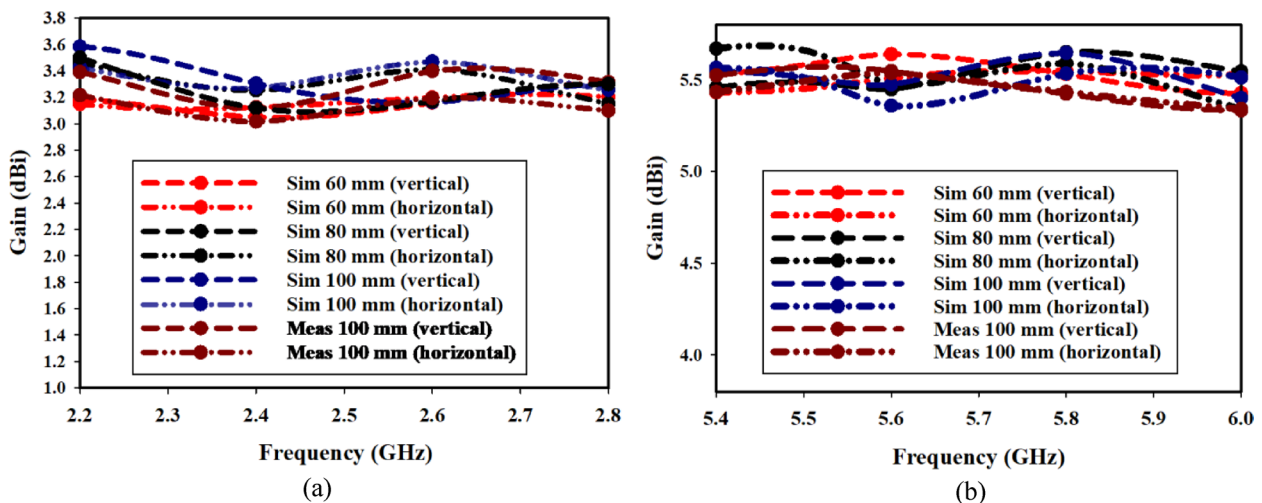


Fig. 24. Gain under bending conditions for different diameters **(a)** 2.4 GHz **(b)** 5.8 GHz.

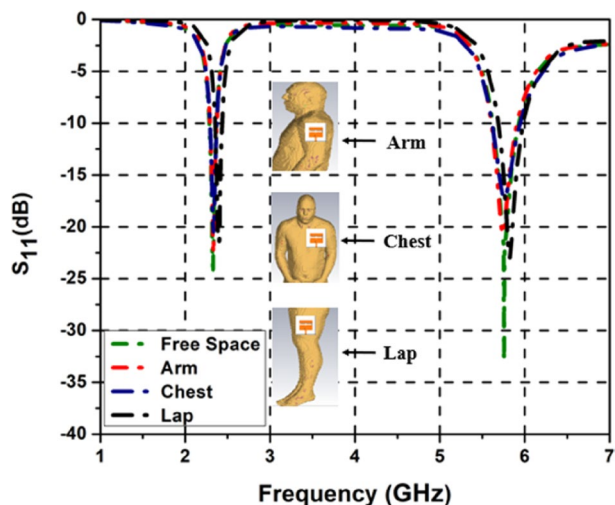


Fig. 25. The simulated S_{11} for the antenna in different scenarios: Free space, arm, chest, and lap.

effects on the substrate materials. As shown in Fig. 23, the gain was also measured under bending conditions in an anechoic chamber. In Fig. 24a, the measured and simulated gain at 2.4 GHz under bending conditions ranges between 3.0 dBi and 3.8 dBi in both the vertical and horizontal planes. Similarly, as shown in Fig. 24b, the measured and simulated gain at 5.8 GHz under bending conditions varies between 5.2 dBi and 5.8 dBi in both the vertical and horizontal planes. Despite the bending, the antenna's performance in terms of simulated and measured gain remained unaffected. These results demonstrate that bending minimally impacts efficiency, ensuring reliable performance in real-world scenarios.

Antenna's performance on human body

The antenna's performance was evaluated under on-body placements (chest, arm, lap) to assess its robustness in real-world biomedical scenarios, and it is noteworthy that all the on-body measurements conducted in this study were non-invasive and posed no risk of harm to the participants. The study protocol was reviewed and approved by the Human Research Ethics Committee of Bayero University, Kano (Approval Number: BUKHREC/WV/044/2025). Informed consent was obtained from all participants prior to their involvement in the study. All procedures were carried out in full accordance with applicable institutional guidelines and national regulations governing human subject research. Figure 25 illustrates the simulated S_{11} parameters for the antenna positioned on the chest, arm, lap, and in free space using CST MWS software. The dual-band operation at 2.4 GHz and 5.8 GHz exhibited only minor frequency shifts, which do not substantially affect performance, as both bands remain above the -10 dB threshold.

Additionally, S_{11} measurements were taken with the antenna placed on various body parts, such as the chest, arm, and lap. The positions were chosen based on: Chest (heart rate monitoring), arm (wearable device

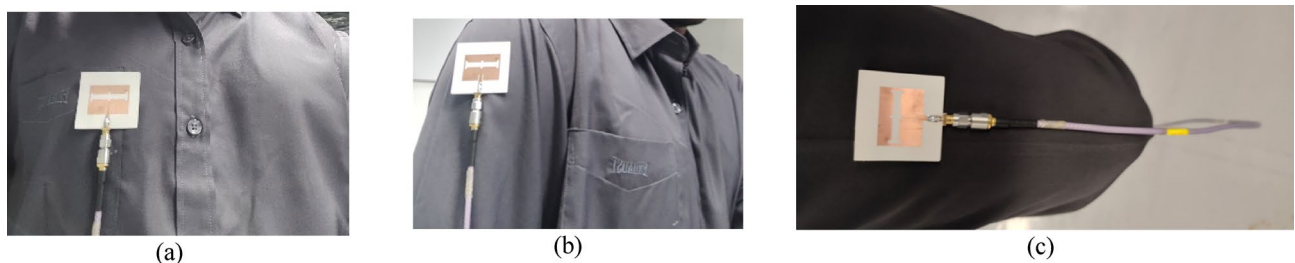


Fig. 26. Placement of the antenna on various parts of human body: (a) chest (b) arm (c) lap.

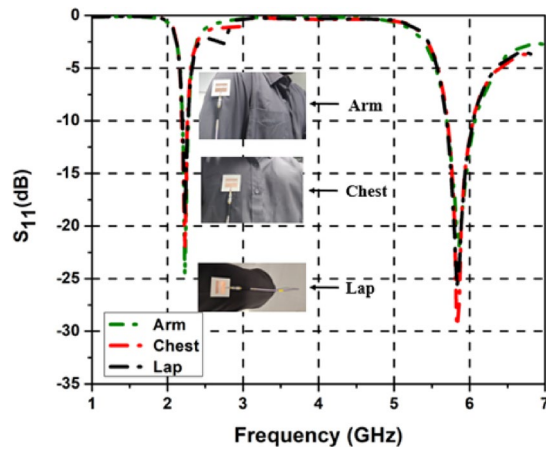


Fig. 27. The measured S_{11} for the antenna on different body locations: arm, chest, and lap.

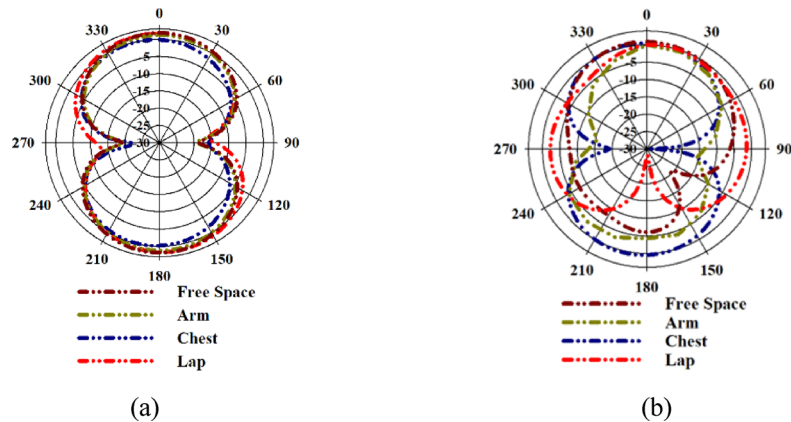


Fig. 28. Radiation pattern of the antenna on various parts of human body (a) 2.4 GHz (b) 5.8 GHz.

placement), and lap (mobility-focused applications) are common sites for biomedical sensors, as shown in Fig. 26.

Figure 27 presents the measured S_{11} values, revealing a slight shift when the antenna is positioned on the arm. This shift is due to the higher dielectric constant of human tissues⁷³, which causes changes in the lower resonant frequency. Furthermore, simulations of the radiation patterns in the E -plane were performed with the antenna placed on different body parts, including the chest, arm, and lap. As shown in Fig. 28, the radiation patterns at both 2.4 GHz and 5.8 GHz exhibit only minor variations, indicating that the antenna's radiation characteristics are largely unaffected by its placement on the body. Figure 28 illustrates the simulated gain variations when the antenna is positioned on the arm, chest, and lap. At 2.4 GHz, the simulated gain ranges from 4.2 dBi to 4.7 dBi, as shown in Fig. 29a. At 5.8 GHz, the gain ranges from 5.0 dBi to 5.2 dBi, as shown in Fig. 29b. These results demonstrate that the antenna maintains stable and satisfactory performance across different body placements, ensuring reliable signal transmission and reception for wearable applications.

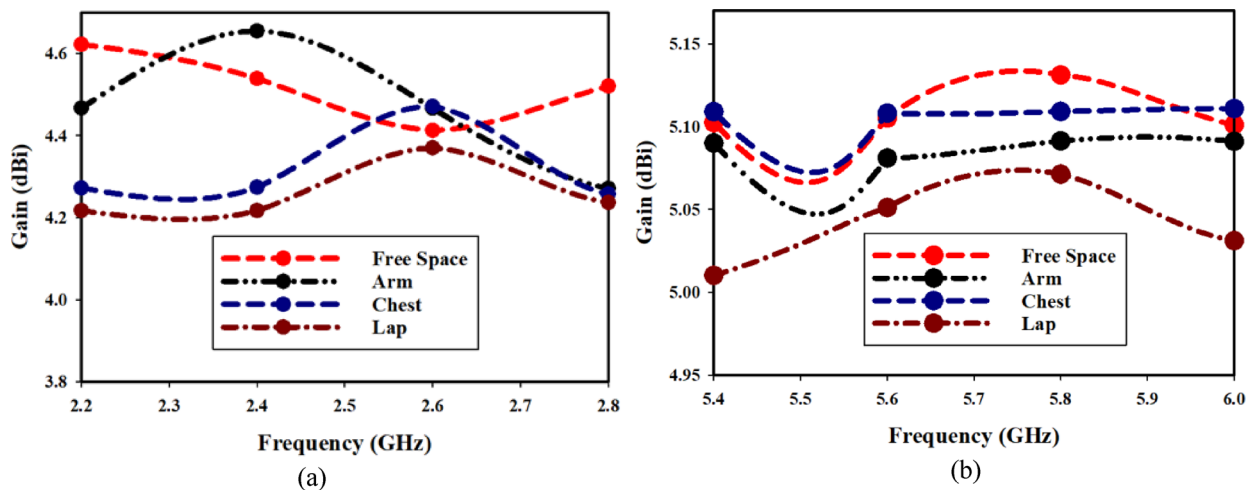


Fig. 29. Gain variation of the antenna on various parts of human body (a) 2.4 GHz (b) 5.8 GHz.

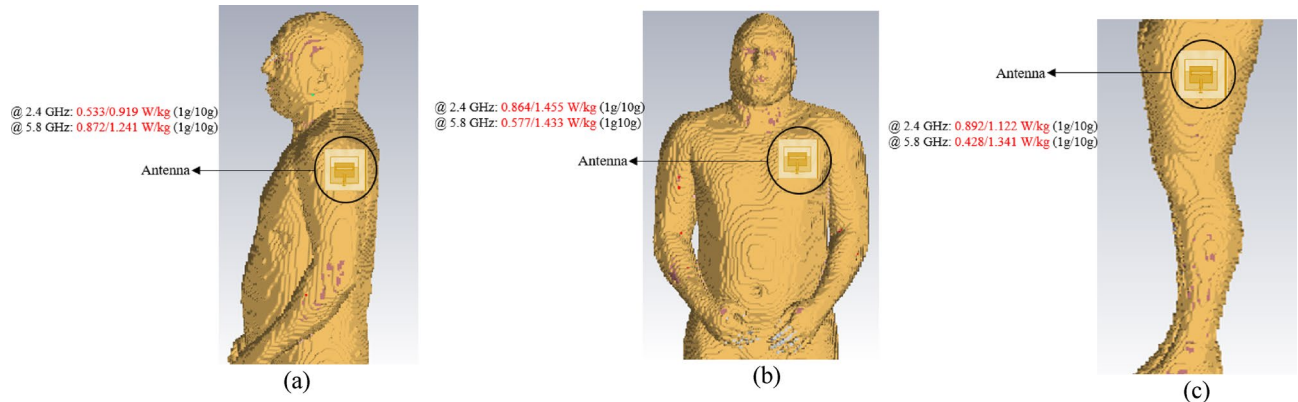


Fig. 30. Simulated SAR values (a) Arm (b) Chest (c) Lap.

SAR analysis

Performing SAR analysis is crucial for wearable antennas to ensure user safety by measuring the RF energy absorbed by the body⁷⁴. SAR quantifies the rate at which RF energy is absorbed per unit mass of tissue, offering insight into potential biological effects⁷⁵. Regulatory organizations such as the FCC and ICNIRP establish safety limits for SAR, which should not exceed 1.6 W/kg for 1 g of tissue and 2 W/kg for 10 g of tissue⁷⁶. These limits are determined based on IEEE C95.1 guidelines and are computed using the CST MWS software environment^{77,78}. To accurately evaluate SAR levels, the antenna's performance was tested on a human phantom model comprised of four layers: skin, fat, muscles, and bones. As shown in Fig. 30, CST MWS simulations evaluated the SAR of the proposed wearable antenna on three body placements (Arm, Chest, Lap) at 5 mm distance. At 2.4 GHz, 1g/10g SAR values were: Arm (0.533 W/kg; 0.919 W/kg), Chest (0.864 W/kg; 1.455 W/kg), Lap (0.892 W/kg; 1.122 W/kg). At 5.8 GHz, results were: Arm (0.872 W/kg; 1.241 W/kg), Chest (0.577 W/kg; 1.433 W/kg), Lap (0.428 W/kg; 1.341 W/kg). These results confirm that the antenna complies with FCC and ICNIRP SAR safety standards.

Experimental validation of the proposed antenna

This section discusses the design and development of a wireless healthcare monitoring system using IoT to validate the proposed wearable dual-band antenna. The system is designed to gather data on patient's heart rates and body temperatures. Wearable antennas are widely used in healthcare monitoring systems to enable continuous tracking⁷⁹. Since the data collected by such systems is essential for accurate diagnosis and treatment, its validation is critical to ensure patient safety and well-being.

Experimental setup

A functional prototype was developed using a SEN11547 pulse sensor and an LM35 temperature sensor from SparkFun Electronics to measure heart rate and body temperature as seen in Fig. 31. Once these vital parameters are recorded, they are transmitted and stored in the ThingSpeak application's database via a NodeMCU ESP-32S Wi-Fi module connected to the proposed antenna. This allows for further analysis or long-term storage,

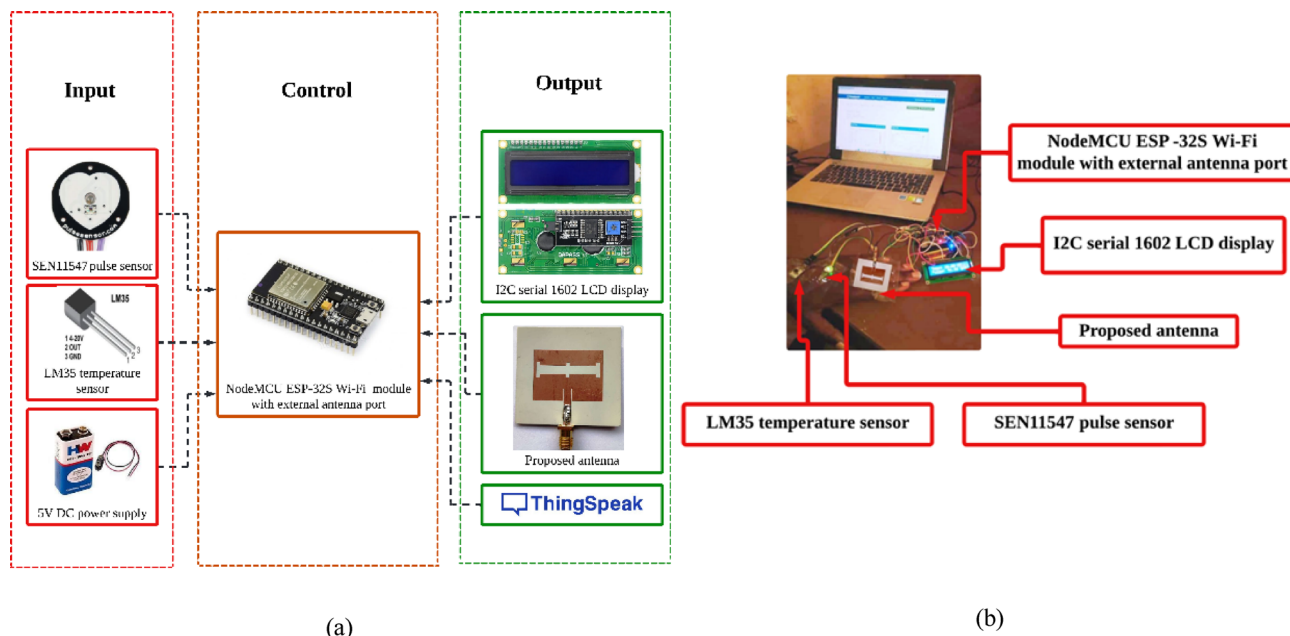


Fig. 31. (a) System block diagram (b) validation setup.

benefiting both patients and medical personnel. The goal of this monitoring system is to automate the collection of vital signs, enhancing healthcare services. The system simplifies processes for patients, caregivers, physicians, and other medical staff. Figure 31a presents the complete block diagram of the wireless healthcare monitoring system. The system is controlled by a NodeMCU ESP-32S Wi-Fi module, which is connected to the proposed antenna and serves as the main control unit. The key input components, the SEN11547 pulse sensor and LM35 temperature sensor, send signals to the microcontroller for processing. The healthcare monitoring system is centered around a NodeMCU ESP-32S Wi-Fi module, which acts as the core control unit and interfaces with the antenna for wireless communication. The SEN11547 pulse sensor and LM35 temperature sensor transmit physiological signals to the microcontroller, where the data is processed into actionable medical metrics. The processed medical data is then sent to an output, which is displayed on the I2C Serial Interface 1602 LCD module. Figure 31b shows the experimental setup. The microcontroller processes the medical data and sends the results to both the I2C Serial Interface 1602 LCD module for display and the ThingSpeak application for database storage.

Performance assessment of the proposed system

To conduct the experiment, a healthy volunteer was selected to measure heart rate and body temperature using the proposed system which was connected to his hand. The volunteer's data was recorded over a 10-min period with measurements taken every minute, resulting in 10 samples, while the volunteer remained in a relaxed state, not engaging in any physical activity. Experiments were conducted in a controlled environment: temperature: 37°C , humidity: $50 \pm 5\%$, electromagnetic interference (EMI) Mitigation: Absence of active RF sources (e.g., microwaves, other Wi-Fi devices). Figure 32 presents graphical representations of the volunteer's heart rate and body temperature. The heart rate data, collected using the healthcare monitoring system with the proposed antenna, shows that the volunteer's heart rate ranged from 65 to 99 BPM. Despite fluctuations, all values fall within the normal range for adults, which is between 60 and 100 BPM⁸⁰. Body temperature data was also retrieved to assess the volunteer's condition. As expected, an increase in body temperature corresponds to a rise in heart rate, and vice versa. The temperature values ranged from 30 to 37°C , which aligns with the healthy range for adults, typically between 30 and 38°C ⁸⁰. However, some readings may fall slightly below or above this range, potentially due to factors such as individual variability, recent activity, or environmental conditions. The antenna's high radiation efficiency (92%) and stable gain (3.8–6.0 dBi) minimized data loss (< 1%) and ensured reliable transmission.

Table 6 provides a comparison between the dual-band antenna developed in this work and previous wearable antennas, highlighting key parameters such as ML model, operating frequency, substrate material, SAR values, efficiency, and gain. While ML is widely used, Performance evaluation of the models employs metrics such as MAE, MSE, RMSLE and R^2 . The ensemble regression model outperformed others, delivering the lowest errors (MAE: 0.83%, MSE: 1.64%, RMSLE: 0.56%, RMSE: 1.83%, MSLE: 0.44%) and the highest accuracy (R^2 : 97.79%), while reducing computational time by 70% compared to conventional CST MWS simulations a leap in efficiency not yet reported in wearable antenna literature^{74,81,82}. Unlike single-algorithm ML studies, the ensemble method mitigates overfitting and enhances robustness for complex dual-band geometries. The centrally slotted patch achieves dual-band operation (2.4/5.8 GHz) on a $40 \times 41 \text{ mm}^2$ footprint, resolving the trade-off between compactness and performance. Additionally, it is noticeable that the existing antenna sizes

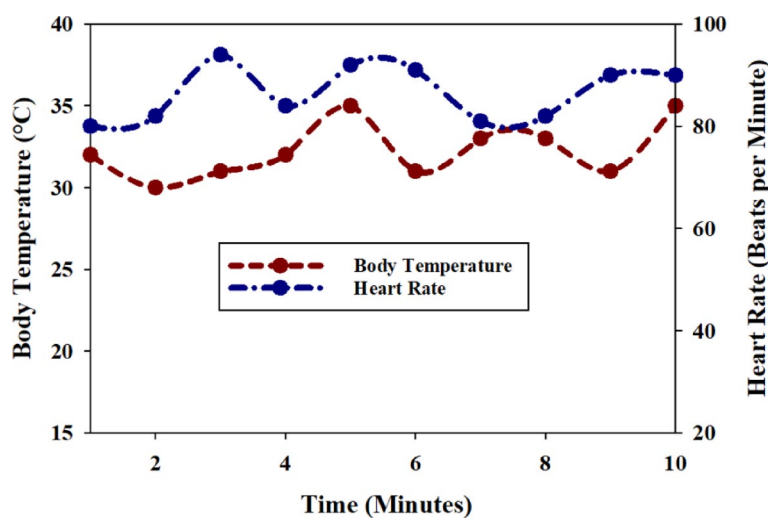


Fig. 32. Comparison of body temperature and heart rate measurements with the proposed antenna.

References	Size (mm ²)	Frequency (GHz)	Material	Bandwidth (%)	Gain (dBi)	SAR (W/kg)	Efficiency (%)	ML prediction/validation
⁴⁷	80 × 60	0.87/0.9	Rogers	NA	2.06/2.12	1.43/1.34	96/99	Yes/Yes
⁷⁴	66.5 × 55	2.45	Rogers	NA	5.61	0.249/0.137	NA	No/No
¹⁶	50 × 50	0.915/0.923	Rogers	NA	1.9/2	0.94/0.85	98/96	Yes/Yes
⁸³	120 × 60	3.0–4.2	Rogers	34.3	4	NA	95	Yes/No
⁸¹	50 × 50	3.5	Rogers	0.62	6.27	0.263/0.076	NA	No/No
⁴⁶	42 × 40	0.87/0.9	FR-4	NA	1.9/2	NA	NA	Yes/Yes
⁸⁴	22 × 33	2.4/3.5	Rogers	NA	0.9/4.7	NA	NA	Yes/No
⁴⁵	75 × 100	2.4	FR-4	14.8	6.7	NA	89.9	Yes/No
⁸²	66 × 55	2.185	Rogers	NA	5.57	0.096/0.076	NA	No/No
⁸⁵	40 × 28	2.4/5.8	Felt	29/18	2/4.96	1.37/1.12	NA	Yes/No
This work	40 × 41	2.4/5.8	Rogers	4.5/2.95	3.8/6.0	0.533/0.872	92/91.7	Yes/Yes

Table 6. The proposed antenna in contrast with the antennas in earlier research. NA, not available.

in references^{45,47,74,81–83} are generally larger in dimensions than the proposed dual-band antennas in this study. Unlike rigid designs^{45,46} the proposed antenna maintains $< - 10$ dB reflection coefficients under bending (60–100 mm radii) and delivers 92% radiation efficiency. Crucially, dual-validation of SAR limits (0.57–0.98 W/kg, FCC/ICNIRP compliant ensures safety, a step often omitted in prior works in^{45,46,83,84}. While 2.4/5.8 GHz ISM bands are standard, the proposed work advances real-world applicability by integrating the antenna into a functional IoT system with SEN11547/LM35 sensors. This system enables continuous, real-time monitoring of vital signs (10-min trials, $< 1\%$ data loss), a practical milestone absent in prior studies^{82,85}.

Conclusion

This work presents a dual-band wearable antenna optimized by ML for biomedical applications and healthcare monitoring systems. Fabricated on a Rogers substrate of 40×41 mm², the antenna operates at 2.4 GHz and 5.8 GHz, the measured impedance bandwidths are 4.5% at 2.4 GHz and 2.95% at 5.8 GHz. At the lower resonance frequency, the radiation efficiency is 92%, and at the upper resonant frequency, it is 91.7%. Regarding radiation patterns, the *E*-plane exhibits directional and bidirectional patterns, whereas the *H*-plane exhibits omnidirectional patterns at the lower and upper resonant frequencies, respectively. To evaluate the antenna's suitability for biomedical applications, the SAR evaluations were carried out to guarantee the antenna's safety for biomedical usage. CST MWS simulations assessed the SAR of the proposed wearable antenna at 5 mm distances on the arm, chest, and lap. The 1g/10g SAR values at 2.4 GHz were 0.864/1.455 W/kg for the chest, 0.892/1.122 W/kg for the lap, and 0.533/0.919 W/kg for the arm. The results were well within safety limits at 5.8 GHz: 0.872/1.241 W/kg (arm), 0.577/1.433 W/kg (chest), and 0.428/1.341 W/kg (lap). Furthermore, bending tests were performed on the antenna while it was worn on the arm, chest, and lap. The results demonstrated that bending had less effect on the antenna's performance. A SEN11547 pulse sensor and an LM35 temperature sensor are included in the proposed healthcare monitoring system to detect body temperature and heart rate. The NodeMCU ESP-32S Wi-Fi module is used to send the data to the ThingSpeak IoT platform, guaranteeing real-time data availability. Measurements were made at one-minute intervals for ten minutes in order to gather experimental data from a volunteer. The body temperature ranged from 30 °C to 37 °C, while the heart rate

varied between 65 and 99 beats per minute. A supervised ML regression approach was successfully applied to predict the antenna's S_{11} . Model performance was assessed using various metrics, including MAE, MSE, RMSLE, MSLE, and the coefficient of determination (R^2). Among the evaluated models, the ensemble regression model achieved the best performance, yielding the lowest errors (MAE: 0.83%, MSE: 1.64%, RMSLE: 0.56%, RMSE: 1.83%, MSLE: 0.44%) and the highest accuracy (R^2 : 97.79%). It also reduced computational time by 70% compared to traditional techniques. These findings confirm the successful deployment of the dual-band antenna within an IoT-based healthcare monitoring system, highlighting its effectiveness and reliability.

Data availability

The datasets generated and/or analyzed during the current study are available from the corresponding author upon reasonable request.

Received: 1 June 2025; Accepted: 12 August 2025

Published online: 22 August 2025

References

- Verma, D. et al. Internet of things (IoT) in nano-integrated wearable biosensor devices for healthcare applications. *Biosens. Bioelectron. X* **11**, 100153 (2022).
- Kaidi, H. M., Izhar, M. A. M., Dzilyauddin, R. A., Shaiful, N. E. & Ahmad, R. A comprehensive review on wireless healthcare monitoring: System components. *IEEE Access* **12**, 35008–35032 (2024).
- Bhatia, D., Paul, S., Acharyya, T. & Ramacharya, S. S. Biosensors and their widespread impact on human health. *Sensors Int.* **5**, 100257 (2024).
- Musa, U. et al. Design and implementation of active antennas for IoT-based healthcare monitoring system. *IEEE Access* **12**, 48453–48471 (2024).
- Gupta, V. & Kumar, R. Biomedical telemetry antenna innovations: Progress, uses, and prospects for the future. *Prog. Electromagn. Res. B* **106**, 85–99 (2024).
- Díaz-Jiménez, D., López, J. L., González-Lama, J. & Espinilla, M. A new horizon in healthcare: An innovative methodology for sensor-based adherence platforms in home monitoring of key treatment indicators. *IEEE Internet Things J.* <https://doi.org/10.1109/JIOT.2024.3424905> (2024).
- Izhar, M. et al. Enhancing healthcare efficacy through IoT-edge fusion: A novel approach for smart health monitoring and diagnosis. *IEEE Access* **11**, 136456–136467 (2023).
- Nemati, M., Ansary, J. & Nemati, N. Machine-learning approaches in COVID-19 survival analysis and discharge-time likelihood prediction using clinical data. *Patterns* **1**, 100074 (2020).
- Su, Y. et al. Printable, highly sensitive flexible temperature sensors for human body temperature monitoring: A review. *Nanoscale Res. Lett.* **15**, 200 (2020).
- Zhumayeva, M., Dautov, K., Hashmi, M. & Nauryzbayev, G. Wireless energy and information transfer in WBAN: A comprehensive state-of-the-art review. *Alexandria Eng. J.* **85**, 261–285 (2023).
- Musa, U. et al. Recent advancement of wearable reconfigurable antenna technologies: A review. *IEEE Access* **10**, 121831–121863 (2022).
- Erdem, A., Eksin, E., Senturk, H., Yildiz, E. & Maral, M. Recent developments in wearable biosensors for healthcare and biomedical applications. *TrAC Trends Anal. Chem.* **171**, 117510 (2024).
- Kher, D. R. & Patel, D. A comprehensive review on wearable health monitoring systems. *Open Biomed. Eng. J.* **15**, 213–225 (2021).
- Ali, U., Ullah, S., Kamal, B., Matekovits, L. & Altaf, A. Design, analysis and applications of wearable antennas: A review. *IEEE Access* **11**, 14458–14486 (2023).
- Ramesh Varma, D. et al. Design of fabric antennas for body protective garment applications and analysis on their performance. *Mater. Today Proc.* **80**, 1538–1547 (2023).
- Yahya, M. S., Soeung, S., Abdul Rahim, S. K., Geok, T. K. & Musa, U. Machine learning-optimized wearable antenna for LoRa localization. *IEEE Access* <https://doi.org/10.1109/ACCESS.2024.3457808> (2024).
- Sharon Giftry, A. L., Kommuri, U. K. & Dwivedi, R. P. Flexible and wearable antenna for biomedical application: Progress and opportunity. *IEEE Access* **12**, 90016–90040 (2024).
- Venkatachalam, D. et al. Compact flexible planar antennas for biomedical applications: Insight into materials and systems design. *Bioengineering* **10**, 1137 (2023).
- Musa, U. et al. Wearable dual-band frequency reconfigurable patch antenna for WBAN applications. *Prog. Electromagn. Res. M* **120**, 95–111 (2023).
- Musa, U. et al. Design and analysis of a compact dual-band wearable antenna for WBAN applications. *IEEE Access* **11**, 30996–31009 (2023).
- Ashyap, A. Y. I. et al. Fully fabric high impedance surface-enabled antenna for wearable medical applications. *IEEE Access* **9**, 6948–6960 (2021).
- Le, T. T. & Yun, T.-Y. Wearable dual-band high-gain low-SAR antenna for off-body communication. *IEEE Antennas Wirel. Propag. Lett.* **20**, 1175–1179 (2021).
- Segun, A. & Telukdarie, A. Revolutionizing healthcare delivery through wireless wearable antenna frameworks: current trends and future prospects. *IEEE Access* **11**, 80327–80347 (2023).
- Geyikoglu, M. D. A novel UWB flexible antenna with dual notch bands for wearable biomedical devices. *Analog Integr. Circuits Signal Process.* **114**, 3 (2023).
- Vinodan, K., Reghu, R., Zacharia, S., Sonia, A. K. & John, A. S. Low profile microstrip patch antennas for wearable medical imaging application. in *2022 International Conference on Emerging Trends in Engineering and Medical Sciences (ICETEMS) 20–23* (2022). <https://doi.org/10.1109/ICETEMS56252.2022.10093443>.
- Srinivas, M. S. S. et al. Multi slot wearable patch antenna for wireless applications. in *2024 IEEE Wireless Antenna and Microwave Symposium (WAMS) 1–4* (2024). <https://doi.org/10.1109/WAMS59642.2024.10527935>.
- Koohestani, M., Azadi-Tinat, N. & Skrjervik, A. K. Compact slit-loaded ACS-fed monopole antenna for bluetooth and UWB systems with WLAN band-stop capability. *IEEE Access* **11**, 7540–7550 (2023).
- Zhang, H., Sun, T., Ren, W., Yuan, C. & Chen, D. A novel dual-band printed monopole antenna with modified SIR loading. *IEEE Access* **12**, 13893–13899 (2024).
- Yao, X., Tong, L. & Cui, Y. A planar inverted-F antenna-based chemical sensor for ion concentrations. *Sens. Actuators Rep.* **2**, 100006 (2020).
- Zulkifli, M. S. et al. Experimental wireless link and SAR assessments of an implantable PIFA for biotelemetry in the 24.5 GHz band. *IEEE J. Electromagn. RF Microwaves Med. Biol.* **7**, 281–289 (2023).

31. Dang, Q. H., Chen, S. J., Nguyen-Trong, N. & Fumeaux, C. Multifunctional reconfigurable wearable textile antennas using coplanar reconfiguration modules. *IEEE Trans. Antennas Propag.* **71**, 3806–3815 (2023).
32. Chung, M.-A., Lin, C.-W., Yang, C.-W. & Mei, I.-P. Wearable reconfigurable antennas with multi-mode switching for sub-6GHz, V-band, and D-band applications. *IEEE Access* **12**, 115448–115464 (2024).
33. Paliwal, R., Srivastava, S. & Budhiraja, R. Customizable substrate integrated waveguide based dual pole band pass filter for X band application. *Prog. Electromagn. Res. M* **125**, 11–19 (2024).
34. Jocqué, J., Verhaeveret, J., Van Torre, P. & Rogier, H. Wearable coupled-quarter-mode SIW antenna platform with hybrid kinetic and ambient-light energy harvesting. *Sci. Rep.* **13**, 5000 (2023).
35. Wang, X., Liu, Z. & Zhang, T. Flexible sensing electronics for wearable/attachable health monitoring. *Small* **13**, 1602790 (2017).
36. Yunusa, Z. A compact low-profile P-shaped wearable antenna for medical application. *Prog. Electromagn. Res. M* **119**, 161–175 (2023).
37. Kaur, M. & Singh, J. ANN based design of hybrid fractal antenna for biomedical applications. *Int. J. Electron.* **106**, 1184–1199 (2019).
38. Marasco, I. et al. Wearable heart rate monitoring device communicating in 5G ISM band for IoHT. *Bioengineering* **10**, 113 (2023).
39. Dakir, R. et al. A new compact and miniaturized multiband uniplanar CPW-fed Monopole antenna with T-slot inverted for multiple wireless applications. *Int. J. Microw. Wirel. Technol.* **9**, 1–5 (2017).
40. Lin, C.-H., Saito, K., Takahashi, M. & Ito, K. A compact planar inverted-F antenna for 2.45 GHz on-body communications. *IEEE Trans. Antennas Propag.* **60**, 4422–4426 (2012).
41. Li, Y. et al. Switchable quarter-wave plate and half-wave plate based on phase-change metasurface. *IEEE Photonics J.* **12**, 1–10 (2020).
42. Ćibiraitė-Lukenskiénė, D. et al. Passive detection and imaging of human body radiation using an uncooled field-effect transistor-based THz detector. *Sensors* **20**, 4087 (2020).
43. Chu, H., Wang, P.-J., Zhu, X.-H. & Hong, H. Antenna-in-package design and robust test for the link between wireless ingestible capsule and smart phone. *IEEE Access* **7**, 35231–35241 (2019).
44. Xu, L.-J., Jin, X., Hua, D., Lu, W. & Duan, Z. Realization of circular polarization and gain enhancement for implantable antenna. *IEEE Access* **8**, 1 (2020).
45. Haque, M. A. et al. Machine learning-based technique for resonance and directivity prediction of UMTS LTE band quasi Yagi antenna. *Heliyon* **9**, e19548 (2023).
46. Yahya, M. S. et al. Machine learning-optimized compact frequency reconfigurable antenna with RSSI enhancement for long-range applications. *IEEE Access* <https://doi.org/10.1109/ACCESS.2024.3355145> (2024).
47. Waly, M. I. et al. Optimization of a compact wearable LoRa patch antenna for vital sign monitoring in WBAN medical applications using machine learning. *IEEE Access* **12**, 103860–103879 (2024).
48. Sharma, Y., Zhang, H. H. & Xin, H. Machine learning techniques for optimizing design of double T-shaped monopole antenna. *IEEE Trans. Antennas Propag.* **68**, 5658–5663 (2020).
49. Zhang, J., Xu, J., Chen, Q. & Li, H. Machine-learning-assisted antenna optimization with data augmentation. *IEEE Antennas Wirel. Propag. Lett.* **22**, 1932–1936 (2023).
50. Cui, L., Zhang, Y., Zhang, R. & Liu, Q. H. A modified efficient KNN method for antenna optimization and design. *IEEE Trans. Antennas Propag.* **68**, 6858–6866 (2020).
51. Rai, J. K. et al. High-gain triple-band T-shaped dielectric resonator based hybrid two-element MIMO antenna for 5G new radio, Wi-Fi 6, V2X, and C-band applications with a machine learning approach. *Int. J. Commun. Syst.* **38**, e6038 (2025).
52. El Misilmani, H. M., Naous, T. & Al Khatib, S. K. A review on the design and optimization of antennas using machine learning algorithms and techniques. *Int. J. RF Microw. Comput. Eng.* **30**, e22356 (2020).
53. Khan, M. M., Hossain, S., Mozumdar, P., Akter, S. & Ashique, R. H. A review on machine learning and deep learning for various antenna design applications. *Heliyon* **8**, e09317 (2022).
54. Jain, R., Thakare, V. V. & Singhal, P. K. Employing machine learning models to predict return loss precisely in 5G antenna. *Prog. Electromagn. Res. M* **118**, 151–161 (2023).
55. Deshmukh, A. A., Mhatre, A., Kudoo, C. & Pawar, S. E-shape microstrip antenna backed by pairs of slots cut ground plane for wideband response. *Procedia Comput. Sci.* **143**, 101–107 (2018).
56. Haque, M. A. et al. Machine learning-based novel-shaped THz MIMO antenna with a slotted ground plane for future 6G applications. *Sci. Rep.* **14**, 32162 (2024).
57. Nahin, K. et al. Performance prediction and optimization of a high-efficiency tessellated diamond fractal MIMO antenna for terahertz 6G communication using machine learning approaches. *Sci. Rep.* **15**, 4215 (2025).
58. Haque, M. A. et al. Multiband THz MIMO antenna with regression machine learning techniques for isolation prediction in IoT applications. *Sci. Rep.* **15**, 7701 (2025).
59. Koziel, S., Pietrenko-Dąbrowska, A. & Leifsson, L. Antenna optimization using machine learning with reduced-dimensionality surrogates. *Sci. Rep.* **14**, 21567 (2024).
60. Haque, M. A. et al. Machine learning based compact MIMO antenna array for 38 GHz millimeter wave application with robust isolation and high efficiency performance. *Results Eng.* **25**, 104006 (2025).
61. Wu, Q., Cao, Y., Wang, H. & Hong, W. Machine-learning-assisted optimization and its application to antenna designs: Opportunities and challenges. *China Commun.* **17**, 152–164 (2020).
62. Czajkowski, M., Jurczuk, K. & Kretowski, M. Steering the interpretability of decision trees using lasso regression - an evolutionary perspective. *Inf. Sci. Ny.* **638**, 118944 (2023).
63. Caron, A., Baio, G. & Manolopoulos, I. Estimating individual treatment effects using non-parametric regression models: A review. *J. R. Stat. Soc. Ser. A Stat. Soc.* **185**, 1115–1149 (2022).
64. Haque, M. A. et al. Machine learning-based technique for gain prediction of mm-wave miniaturized 5G MIMO slotted antenna array with high isolation characteristics. *Sci. Rep.* **15**, 276 (2025).
65. Lei, T. M. T., Ng, S. C. W. & Siu, S. W. I. Application of ANN, XGBoost, and other ML methods to forecast air quality in macau. *Sustainability* **15**, 5341 (2023).
66. Ferrouhi, E. M. & Bouabdallaoui, I. A comparative study of ensemble learning algorithms for high-frequency trading. *Sci. African* **24**, e02161 (2024).
67. Musa, U. et al. Investigation of the nonlinearity of PIN diode on frequency reconfigurable patch antenna. *J. Eng.* **2023**, e12308 (2023).
68. Zhou, L., Fang, S. & Jia, X. Dual-band and dual-polarised circular patch textile antenna for on-/off-body WBAN applications. *IET Microwav. Antennas Propag.* **14**, 643–648 (2020).
69. Bhattacharjee, S., Maity, S., Chaudhuri, S. R. B. & Mitra, M. A compact dual-band dual-polarized omnidirectional antenna for on-body applications. *IEEE Trans. Antennas Propag.* **67**, 5044–5053 (2019).
70. Zhou, L., Fang, S.-J. & Jia, X. A compact dual-band and dual-polarized antenna integrated into textile for wban dual-mode applications. *Prog. Electromagn. Res. Lett.* **91**, 153–161 (2020).
71. Xiaomu, H., Yan, S. & Vandenbergbosch, G. A. E. Wearable button antenna for dual-band WLAN applications with combined on and off-body radiation patterns. *IEEE Trans. Antennas Propag.* **65**, 1384–1387 (2017).
72. Waly, M. I. et al. Advancement of a high-efficiency wearable antenna enabling wireless body area networks. *IEEE Access* **11**, 138325–138335 (2023).

73. Ashyap, A., Raad, R., Tubbal, F., Khan, W. A. & Abulgaseem, S. Comprehensive review of wearable antennas with flexible periodic structures for body-effect mitigation. *IEEE Access* **13**, 22590–22636 (2025).
74. Soni, G., Yadav, D., Kumar, A., Jain, P. & Rathi, A. Design and SAR analysis of DGS based deformed microstrip antenna for ON/OFF body smart wearable IoT applications. *Phys. Scr.* **100**, 015536 (2024).
75. Wang, X., Huang, S. Y. & Yucel, A. C. Uncertainty quantification in SAR induced by ultra-high-field MRI RF coil via high-dimensional model representation. *Bioengineering* **11**, 730 (2024).
76. Musa, U. et al. A compact and semi-flexible dual-band patch antenna for IoT-based WBAN applications. in *2024 International Conference on Future Technologies for Smart Society (ICFTSS)* 28–31 (2024). <https://doi.org/10.1109/ICFTSS61109.2024.10691368>.
77. Zhao, C. & Geyi, W. Design of a dual band dual mode antenna for on/off body communications. *Microw. Opt. Technol. Lett.* **62**, 514–520 (2020).
78. Ahmad, S., Ghaffar, A., Hussain, N. & Kim, N. Compact dual-band antenna with paired L-shape slots for on- and off-body wireless communication. *Sensors* **21**, 7953 (2021).
79. Linh, V. T. N. et al. Advances in wearable electronics for monitoring human organs: Bridging external and internal health assessments. *Biomaterials* **314**, 122865 (2025).
80. Afreen Banu, E. & Rajamani, V. Design of online vitals monitor by integrating big data and IoT. *Comput. Syst. Eng.* **44**, 2469–2487 (2023).
81. Soni, G. K., Yadav, D., Kumar, A., Sharma, C. & Yadav, M. V. Flexible ring slot antenna for optimized 5G performance in N77 and N78 frequency bands for wearable applications. *Prog. Electromagn. Res. C* **150**, 47–55 (2024).
82. Soni, G. K., Yadav, D., Kumar, A., Jain, P. & Yadav, M. V. Design and optimization of flexible DGS-based microstrip antenna for wearable devices in the Sub-6 GHz range using the nelder-mead simplex algorithm. *Results Eng.* **24**, 103470 (2024).
83. Dwivedi, A. K. et al. Circularly polarized printed dual port MIMO antenna with polarization diversity optimized by machine learning approach for 5G NR n77/n78 frequency band applications. *Sci. Rep.* **13**, 13994 (2023).
84. Aliyu Babale, S. et al. Machine learning-based optimized 3G/LTE/5G planar wideband antenna with tri-bands filtering notches. *IEEE Access* **12**, 80669–80686 (2024).
85. Merugumalli, R. K., Murugan, N. A. & Chalasani, S. R. Design and optimization of a compact dual-band antenna using artificial neural networks for body area network applications. *AEU Int. J. Electron. Commun.* **200**, 155911 (2025).

Acknowledgements

The author Amor Smida extends the appreciation to the Deanship of Postgraduate Studies and Scientific Research at Majmaah University for funding this research work through the project number (R-2025-1937).

Author contributions

Umar Musa and Muhammad S. Yahya: Conception, design, data collection, initial analysis, simulation, and writing the original manuscript. Amor Smida, Mohamed I. Waly, Jun Jiat Tiang, Nazih Khaddaj Mallat, Surajo Muhammad and Abubakar Salisu: Data interpretation, manuscript review, and editing.

Funding

The authors declare that no financial support was received for the research, authorship, and/or publication of this article.

Declarations

Competing interests

The authors declare no competing interests.

Additional information

Correspondence and requests for materials should be addressed to U.M., A.S. or J.J.T.

Reprints and permissions information is available at www.nature.com/reprints.

Publisher's note Springer Nature remains neutral with regard to jurisdictional claims in published maps and institutional affiliations.

Open Access This article is licensed under a Creative Commons Attribution-NonCommercial-NoDerivatives 4.0 International License, which permits any non-commercial use, sharing, distribution and reproduction in any medium or format, as long as you give appropriate credit to the original author(s) and the source, provide a link to the Creative Commons licence, and indicate if you modified the licensed material. You do not have permission under this licence to share adapted material derived from this article or parts of it. The images or other third party material in this article are included in the article's Creative Commons licence, unless indicated otherwise in a credit line to the material. If material is not included in the article's Creative Commons licence and your intended use is not permitted by statutory regulation or exceeds the permitted use, you will need to obtain permission directly from the copyright holder. To view a copy of this licence, visit <http://creativecommons.org/licenses/by-nc-nd/4.0/>.

© The Author(s) 2025